



# Lawrence Berkeley Laboratory

UNIVERSITY OF CALIFORNIA

## Materials & Molecular Research Division

Submitted to WEAR

THE EROSION BEHAVIOR OF STEEL AS A FUNCTION OF  
MICROSTRUCTURE ON SOLID PARTICLE EROSION

Alan V. Levy

April 1980

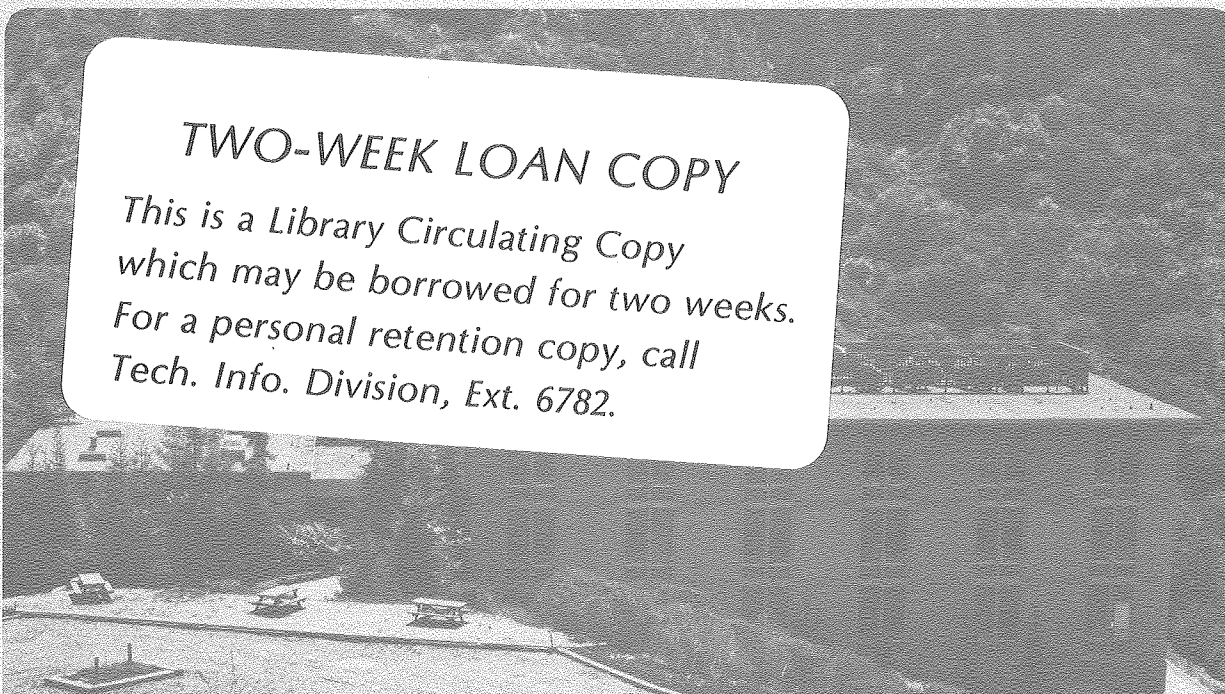
RECEIVED  
LAWRENCE  
BERKELEY LABORATORY

JUL 9 1980

LIBRARY AND  
DOCUMENTS SECTION

### TWO-WEEK LOAN COPY

*This is a Library Circulating Copy  
which may be borrowed for two weeks.  
For a personal retention copy, call  
Tech. Info. Division, Ext. 6782.*



LBL-10798c.2

## **DISCLAIMER**

This document was prepared as an account of work sponsored by the United States Government. While this document is believed to contain correct information, neither the United States Government nor any agency thereof, nor the Regents of the University of California, nor any of their employees, makes any warranty, express or implied, or assumes any legal responsibility for the accuracy, completeness, or usefulness of any information, apparatus, product, or process disclosed, or represents that its use would not infringe privately owned rights. Reference herein to any specific commercial product, process, or service by its trade name, trademark, manufacturer, or otherwise, does not necessarily constitute or imply its endorsement, recommendation, or favoring by the United States Government or any agency thereof, or the Regents of the University of California. The views and opinions of authors expressed herein do not necessarily state or reflect those of the United States Government or any agency thereof or the Regents of the University of California.

THE EROSION BEHAVIOR OF STEEL  
AS A FUNCTION OF MICROSTRUCTURE  
ON SOLID PARTICLE EROSION

ALAN V. LEVY

Materials and Molecular Research Division  
Lawrence Berkeley Laboratory  
University of California  
Berkeley, California 94720

ABSTRACT

The effects of the microstructure of two ductile steels on their solid particle erosion were determined. The steels chosen allowed microstructural changes to be made without drastically changing their hardness, which is reported to be a direct function of erosion resistance. The steels used were plain carbon 1075 and 1020 in the coarse pearlite, fine pearlite, and spheroidized forms for the 1075 and in three spheroidized conditions for the 1020 steel. Single particle and multiple particle erosion tests were conducted using 240  $\mu\text{m}$  diameter SiC particles, angles of impingement of 15°, 30°, and 90° and velocities of 30.5 mps (100fps) and 61 mps (200fps). Both surface and subsurface analyses were conducted using scanning electron microscopy.

In the room temperature erosion tests, the spheroidized microstructure of the 1075 steel eroded less than either of the two pearlitic microstructures. It was found that the pearlitic steels exhibited cracking at the eroded surface as well as beneath it, causing greater material removal. The spheroidized structure showed no surface cracking; however, cracking did occur at a depth of approximately 20  $\mu\text{m}$  below the surface. The carbide particle spacing

in the 1020 spheroidized steel also had a measureable effect on the erosion rate. The hardness of the various microstructures had an inverse relation to the erosion rate.

## ACKNOWLEDGMENT

This work was supported by the Division of Materials Sciences, Office of Basic Energy Sciences, U.S. Department of Energy. Some of the information contained in the unpublished masters thesis of Lorin Brass was used in this paper. Information on the 1020 steel behavior was developed by R. A. Bellman, Jr.

Prepared for the U.S. Department of Energy under Contract W-7405-ENG-48.

## INTRODUCTION

Material removal by moving solid particles carried in fluid streams has been recognized as a serious problem for many years in various engineering applications. Early studies in solid particle erosion were prompted by severe damage to equipment used for the catalytic cracking of oil.<sup>1,2</sup> Since then erosion studies have been conducted for a variety of reasons including dust and sand erosion of helicopter engine compressor blades and small solid particle damage to gas turbine blades.<sup>3,4</sup> More recently, there has been a renewed interest in the field because of the hostile environment to which materials are subjected in many advanced energy conversion systems, especially coal gasification and liquefaction.<sup>5</sup> Severe damage to internal components including piping, fittings, cyclones, and valves has been observed in coal gasification pilot plants caused by coal char moving at velocities up to 30.5 meters/second. It is very important that a better understanding of the solid particle erosion mechanism be obtained.

Previous workers in the field have made valuable advances in the understanding of erosion.<sup>6-15</sup> It has been determined that erosion of ductile alloys strongly depends on particle velocity and angle of impingement,  $\alpha$ , as shown in Fig. 1, and, to a lesser degree on particle size, shape, density and solids loading in the fluid stream. The impingement angle for maximum erosion is usually found to be from 15° to 30° for ductile alloys. Brittle materials behave quite differently than ductile materials (see Fig. 1).

A majority of the work in erosion has been on mechanisms of metal removal with analytical modeling. Not until recently have the metallurgical aspects of erosion been addressed. Consequently, limited efforts have been made to understand what is occurring microstructurally during the erosion process beneath the surface of the material. Ives and Ruff,<sup>16</sup> in a pioneering contribution, conducted a study of erosive single particle impacts on 310 stainless steel and copper using scanning electron microscopy (SEM) and transmission electron microscopy (TEM). They found extremely high dislocation densities in the immediate vicinity of the impact crater, indicative of severe plastic deformation.

It is the purpose of the present work to vary the microstructure of the target material to determine its effect on solid particle erosion and to examine microscopically subsurface deformation caused by the erosion process using SEM. The approach taken was to select steels, 1075 and 1020, that could be readily heat treated into different microstructures without changing drastically the hardness of the material. The steels were chosen because they could be heat treated to a lamellar structure and a spheroidized structure making it possible to examine the effect of fine pearlite, coarse pearlite, and various spheroidized structures on erosion.

## EXPERIMENTAL PROCEDURES

### Specimen Preparation

The commercial plain carbon 1075 and 1020 steels were obtained for erosion testing and cut into samples 0.75 in x 2.5 in x 0.125 in. The 1075 steel was heat treated to fine pearlite, coarse pearlite, and spheroidized microstructures (Fig. 2) in a high vacuum controlled atmosphere furnace to prevent chemical changes on the sample surface. Coarse pearlite was formed by austenitizing at  $875^{\circ} \pm 3^{\circ}\text{C}$  for 30 minutes, furnace cooling to  $700^{\circ} \pm 3^{\circ}\text{C}$  in a stream of argon gas, holding for 3 hours, and furnace cooling to room temperature. Fine pearlite was formed by austenitizing at  $875^{\circ} \pm 3^{\circ}\text{C}$  for 30 minutes, fast cooling to  $600^{\circ} \pm 3^{\circ}\text{C}$  in a stream of argon gas, holding for 30 minutes, and cooling to room temperature. The spheroidized specimens were heat treated by encapsulating the samples in quartz tubes filled with argon, austenitizing at  $875^{\circ} \pm 5^{\circ}\text{C}$  for 30 minutes, furnace cooling to  $700^{\circ}\text{C}$ , holding for 10 days, and air cooling to room temperature.

The 1020 steel was obtained in the hot rolled form, heated to  $950^{\circ}\text{C}$  for one hour for complete austenization, water quenched, polished to 600 grit, enclosed in stainless steel bags with an argon atmosphere, and spheroidized for 10 to 50 hours at  $707^{\circ}\text{C}$  to obtain three different spheroid sizes and distributions.

Characterization of the 1075 steel included determining chemical composition, hardness, and tensile behavior including work hardening coefficient ( $n$ ), and work hardening rates. The work hardening coefficient was determined by plotting log true stress,  $\sigma_t$ , vs. log



true strain,  $\epsilon_t$ , and finding the slope of that line, assuming the data corresponds to the equation  $\sigma - \sigma_y = k(\epsilon - \epsilon_y)^n$ . Work hardening rate was determined by the slope of the tangent of the true stress - true strain curve at 1 percent and 2 percent strain.

Samples used for multiple particle impact testing were metallographically polished through a 4/0 paper prior to testing. Those used for single particle impact studies were polished through 1  $\mu\text{m}$  diamond wheel.

In a series of tests to study the threshold behavior of the erosion of the 1075 steel, specimens were cold rolled to 20, 40, 60, and 80 percent reduction of area.

#### Erosion Testing

The erosion testing was conducted at room temperature using an air blast tester shown in Figs. 3 and 4. The tester operated by feeding the eroding particles from a vibrating hopper into a stream of gas. The particle feed rate was found to be accurate and constant at 20 grams/minute, a solid loading of 0.6 gm SiC/gm air at 30.5 mps (100 fps) and 0.36 gm SiC/gm air at 61 mps (200 fps) for the size and shape of particles used in this study. Angular silicon carbide particles were used as the eroding material having a hardness of about 4500 (VHN) and an actual (true) density of 3.2 grams/cm<sup>3</sup>. Most erosion testing was conducted using +65 -60 mesh (240  $\mu\text{m}$  diameter) particles. The testing device allowed for choice of particle velocity by changing the pressure drop and gas flow rate across a 0.305 m (12") long by 4.77 mm (0.1875") ID stainless steel nozzle. Particle

velocities used in this study were 30.5 mps (100 fps) and 61 mps (200 fps). These velocities were calculated using a one dimensional, two phase flow computer analysis<sup>17</sup> and experimentally verified using a rotary disc testing device.<sup>18</sup> Figure 5 is a schematic showing where the disc was placed and how the velocity calculation was made. Angles of impingement used in this study were 15°, 30°, and 90°.

Single particle and multiple particle erosion tests were conducted on the steel samples. Single particle impact craters were observed with the SEM and stereo photomicrographs were taken to determine the depth of the craters. The multiple particle impact tests were conducted by impacting five, 60 gram charges of SiC on the sample surface for the 1075 steel and five 30 gram charges of SiC for the 1020 steel with weight loss measurements of the sample taken after each 60 or 30 gram charge. After each particle charge impacted, the surface was subjected to a high pressure air blast to minimize the amount of SiC left on the surface before weight measurements were taken. Erosion rates for each successive particle charge of SiC were determined by the formula:

$$\text{Erosion Rate} = \frac{\text{change in mass of sample}}{\text{mass of impacting particles (60 or 30 gm)}}$$

The surface and cross section of the multiple particle eroded samples and single particle impact craters were analyzed microscopically.

## RESULTS

### 1075 Steel

Hardness and tensile data for the 1075 steel are presented in Tables I and II and Fig. 6. The spheroidized steel was somewhat softer ( $R_B$  79) than the coarse pearlite ( $R_B$  90), with the fine pearlite being the hardest ( $R_B$  100). Tensile data show that the spheroidized structure had a slightly lower yield and ultimate strength than the pearlitic steel and greater elongation. The work hardening exponent ( $n$ ) was also much greater for the spheroidized structure. However, the initial work hardening rate (at 1 percent strain) was almost twice as large for the pearlitic steel as for the spheroidized structure.

Results of a typical multiple particle erosion test for the three different microstructures of the 1075 steel are shown in Fig. 7. This curve was made for a test particle velocity of 30.5 mps (100 fps) and an angle of impingement of  $30^\circ$ . The curve shows that after steady state erosion had begun (the horizontal portion of the curve) the spheroidized microstructure eroded less than either the coarse or fine pearlite. It should also be noted that there is a definite threshold region of increasing erosion rate before steady state erosion begins.

Erosion data at a particle velocity of 61 mps (200 fps) also show that the spheroidized structure eroded less than the fine or coarse pearlite structures (see Fig. 8). At 61 mps (200 fps), however, the threshold region is not as pronounced as a particle velocity of 30.5 mps (100 fps).

Table I  
1075 Steel Hardness Data

	R <sub>B</sub>	VHN (1000 gm LOAD)
Fine Pearlite	100	250
Coarse Pearlite	90	191
Spheroidized	79	162
Spheroidized		
Cold Rolled 20%	99	242
Cold Rolled 40%	102	262
Cold Rolled 60%	105	288
Cold Rolled 80%	106	316

Table II

## Tensile Data 1075 Steel

	Yield Strength	Ultimate Strength	% Elongation	Work Hardening Coefficient (n)	Work Hardening Rate at 1% $\epsilon$	Work Hardening Rate at 2% $\epsilon$
Coarse Pearlite	64,000 psi (441.2 MN/m <sup>2</sup> )	126,400 psi (871.8 MN/m <sup>2</sup> )	12.4	0.15	55,500 psi (383 MN/m <sup>2</sup> )	11,100 psi (76.6 MN/m <sup>2</sup> )
Spheroid- ized	32,200 psi (222 MN/m <sup>2</sup> )	78,300 psi (538.2 MN/m <sup>2</sup> )	26.8	0.27	23,800 psi (164 MN/m <sup>2</sup> )	14,800 psi (102 MN/m <sup>2</sup> )

Data from flat tensiles with one inch gauge lengths, 0.151" thick cut transverse to rolling direction (same orientation as erosion samples).

Erosion rates can be compared for the three microstructures at all angles of impingement on erosion rate vs. angle of impingement curves for 30.5 and 61 mps (see Figs. 9 and 10). The curves are typically shaped for ductile alloys. Data scatter bands for 15° and 30° show that the pearlitic steel curves were essentially the same at 30.5 mps (100 fps) velocity while the spheroidized steel curve was lower. For 61 mps (200 fps) the order of performance was the same but the amount of difference in erosion among the microstructures had changed.

A one-half hour duration test was conducted to determine if the pearlitic and spheroidized microstructures behaved the same after longer erosion times. The particle velocity used was 61 mps (200 fps) and the impact angle was 15°. The SiC particle size was slightly larger (280  $\mu$ m diameter) than was used in the tests of Figs. 9 and 10. The spheroidized structure once again eroded less (wt. loss = 0.185 grams) than the pearlitic steel (wt. loss = 0.194 grams). The erosion resistance of the different microstructures is not what would have been expected from hardness data; the erosion increases with increasing hardness rather than decreasing. The fine pearlite material should have eroded the least since it was the hardest of the three microstructures. ( $R_B$  100 compared to  $R_B$  79 for the spheroidized steel).

Results of the single particle impact tests showed that the pearlitic and spheroidized structures exhibited markedly different mechanisms of erosion. The pearlitic steels typically showed fracturing of the cementite plates as the particle impacted the

surface as seen in Figs. 11 and 12. This type of surface fracture would be expected because of the brittleness of the cementite plates. The ferrite matrix, being very soft and ductile, appears to be torn away leaving the plates exposed. The spheroidized steel under single particle impact showed no severe cracking but rather exhibited a mechanism where the ferrite matrix was plastically deformed with carbide particles lying near or on the surface after impact (see Fig. 13).

Cross sections of single particle impact craters resulting from large SiC particle impacts (1200  $\mu\text{m}$  diameter) showed similar results to the SEM analysis of the surface the single particle impact area. The pearlitic steel showed the cementite plates breaking off at the surface, Fig. 14 (the particles appearing above the metal surface are mounting material). It is also interesting to note that the cementite plates below the surface are being bent in the process of crater formation, Fig. 15. The cementite deformation indicates the extent and direction of plastic flow beneath the surface. In many instances these cementite plates were bent without fracturing.

Multiple particle impact test samples in cross section showed microcracks forming below the surface. At particle velocities of 61 mps (200 fps) and 30.5 mps (100 fps) and angles of impingement of  $15^\circ$  and  $30^\circ$ , the spheroidized structure showed cracks at a depth of 20  $\mu\text{m}$ , Fig. 16. These sub-surface cracks are similar to those found by Suh<sup>14</sup> in his studies of sliding wear. Under the same conditions the pearlitic steel showed cracks much nearer the surface (3 to 6  $\mu\text{m}$ ),

Fig. 17. At a  $90^\circ$  impact angle and a particle velocity of 61 mps (200 fps), the spheroidized and pearlitic structures both showed that most of the subsurface cracking occurred in or very near the plastically deformed surface layer. Cracks were seen to a depth of  $\sim 15 \mu\text{m}$  below the surface which is assumed to be the depth of plastic deformation.

The results of cold working of the surface prior to eroding are shown in Table III. As the degree of cold work was increased the erosion rate after the first 60 grams of particles increased.



Table III

1075 Steel Erosion Data, Spheroidized Microstructure

% Cold Work	Initial Erosion Rate (After First 60 Grams of Impacting Particles)
0	$9.8 \times 10^{-3}$ mg/g
20	$10.3 \times 10^{-3}$ mg/g
40	$14.9 \times 10^{-3}$ mg/g
60	$16.6 \times 10^{-3}$ mg/g
80	$17.2 \times 10^{-3}$ mg/g

Steady State Erosion Rate  $\cong 22 \times 10^{-3}$  mg/g

1020 Steel

The three different spheroidal microstructures tested are shown in Figs. 18-20 along with data on their carbide particle sizes and spacings. Grid maps of each microstructure were made to determine their particle spacings and densities. Run 1 (Fig. 18) had the smallest size particles and the shortest interparticle spacing. Run 2 had roughly half the number of carbide particles, twice the average particle size and twice the average particle spacing of Run 1. Run 3 had very large particles compared to Runs 1 and 2, much greater particle spacings and considerably fewer number of particles. Run 1 used the hardest steel,  $R_B$  30, Run 2's steel was slightly softer,  $R_B$  25 and Run 3's steel was considerably softer at  $R_B$  10.

Figure 21 is a curve showing the erosion behavior of the three microstructures. It can be seen that the amount of erosion in Run 2 is 33 percent less than that in Run 1 at the steady state condition. Run 2 has an interparticle spacing twice that of Run 1, providing more soft, ductile ferrite structure between the hard carbide particles to plastically deform upon impact by the eroding SiC particles. The steel in Run 2 has a somewhat lower hardness than that used in Run 1. Run 3, on the other hand, is much softer than the other two runs' steel specimens with a much lower strength to resist erosion. It experienced roughly twice the erosion of the other two spheroidized specimens.

## DISCUSSION

### 1075 Steel

#### Steady State Erosion

The single particle impact study proved to be useful in explaining why the pearlitic structure eroded more than the spheroidized structure. Since the pearlitic steel showed fracturing on the eroded surface it is reasonable to assume the pearlitic steel's mechanism of material loss would be one in which the material could be driven from the surface in the form of chips that have cracked from the surface along brittle cementite lamellae (see Fig. 12). The spheroidized steel showed no surface cracking and therefore would exhibit a mechanism in which much material would be plastically moved about with less material being actually driven from the surface (Fig. 13).

The type of material loss mechanism the spheroidized steel exhibited has also been seen in abrasive wear studies of spheroidized steel.<sup>19</sup> Recall also that the tensile data showed the pearlitic steel had a much lower percent elongation and a much higher initial rate of work hardening than the spheroidized steel. The high strains and strain rates of erosion could cause the pearlitic steel to severely work harden and promote fracture at the surface. The spheroidized structure, on the other hand, being more ductile and having a lower initial rate of work hardening, would not fracture at the surface but could produce a stress system capable of causing cracks below the surface.

Subsurface cracking did appear in the spheroidized samples at a depth of approximately 20  $\mu\text{m}$  and to a lesser degree and nearer the surface in the pearlitic steels. Subsurface cracking has been seen before in sliding wear studies<sup>14</sup> and has been alluded to in erosion studies to account for erosion at high impact angles. A number of theories to explain this cracking under erosion type loading conditions have been given in the literature.<sup>6,7,19</sup> Two possible explanations for the subsurface cracking will be discussed.

1. Finnie<sup>6</sup> and others have indicated in their work that it is possible that a low cycle fatigue phenomenon could be responsible for causing subsurface cracking at high angles of impingement. This type of failure would stem mainly from the alternating normal component of the force acting on the surface which would cause alternating compressive and tensile plastic strains in the material. Cracking would probably begin most quickly and severely in the plastic zone. Once cracks had begun, propagation would cause connection of microcracks and material would spall off.

From the present study it would seem that the low cycle fatigue theory could explain subsurface cracking at normal angles of particle impingement since severe cracking was seen in the plastically deformed region and at what seemed to be the interface of plasticity and elasticity. However, the low cycle fatigue process would not totally explain the subsurface cracking at more grazing angles where the stresses normal to the surface are much lower.

2. Another explanation for subsurface cracking is given by workers on sliding wear.<sup>14</sup> In the delamination theory of wear it is believed there is a certain work-softened layer caused by the wear process due to dislocations near the surface being able to reach the free surface and not cause entanglement and work hardening. However, at a certain depth below the surface, dislocations are no longer able to move to the surface, but instead become entangled and therefore do not transmit the energy of the wear process out to the surface or into the material. At this depth stresses rise that eventually are capable of nucleating cracks, especially at interfaces between incoherent second phase particles and the matrix. It is possible that this explanation could be converted from sliding wear behavior to solid particle erosion where strain rates are much higher than in most other wear processes. However, as has been discussed earlier,<sup>16</sup> high concentrations of dislocations below the surface have been associated with erosive single particle impacts and with cavitation erosion conditions. Further work is needed to determine if the delamination theory of wear could adequately explain the subsurface cracking observed in this investigation.

#### Threshold Behavior

The threshold region of the erosion rate vs. amount of particles curve before steady state erosion has begun may be important in applications where erosion and corrosion are occurring simultaneously. A component may exhibit threshold behavior throughout its life due to

a constant build up and breakdown of the surface material during corrosion and erosion.

The threshold behavior before steady state erosion begins, as seen in Figs. 7 and 8 (curves of Erosion Rate vs. Amount of Impacting Particles), is more pronounced at particle velocities of 30.5 mps (100 fps) than at 61 mps (200 fps). Others have observed this type of behavior at normal angles of impact and have attributed it to eroding particle deposition in the sample.<sup>9</sup> At glancing angles the deposition and therefore the threshold would disappear. In the present study, a low initial erosion rate was observed at all angles of impingement at a particle velocity of 30.5 mps (100 fps) and at 90° at a particle velocity of 61 mps (200 fps). Since the threshold was quite pronounced at glancing angles, it was believed that SiC deposition was not the primary cause for the low initial weight loss.

A test series was performed to provide further insight into the threshold behavior. Samples were cold rolled to 20, 40, 60, and 80 percent reduction, Table III, and eroded by one 60 gm charge of SiC particles at a particle velocity of 30.5 mps (100 fps) at an impingement angle of 15°. As the amount of reduction and corresponding cold work and hardness increased, the amount of erosion also increased. It approached steady state erosion but did not achieve it. However, the amount of erosion between the annealed (0 percent reduction) and the 80 percent reduction specimens almost doubled. The amount of erosion in the threshold period has an inverse relation with work hardening. An explanation for this phenomenon has

been developed in a series of experiments in this laboratory and will be reported in a subsequent paper.

#### 1020 Steel

The three different microstructures used defined the range in which erosion is affected by the distribution and hard particles in a soft, ductile matrix. In Run 1, where the carbide particles were the smallest in size and greatest in quantity and distance between the hard particles, where the soft, ductile ferrite matrix occurred was the smallest, the erosion was greater than in Run 2. In Run 2 the 1/3 less erosion occurred because the brittle spheroids were consolidated into fewer, larger particles with more ductile ferrite between them. This permitted more plastic deformation of the surface to occur without material removal and the erosion was reduced.

In Run 3, the carbide particles had been consolidated to such a degree that they effectively played no role in strengthening the steel and it assumed completely the characteristics of the low strength ferrite matrix. The steel in this condition was now more susceptible to erosion because of its very low strength. Any increase in ductility that was present to permit more plastic deformation without material loss upon particle impacts (as occurred in Run 2 compared to Run 1) was more than offset by the much lower strength which permitted impacting particles to readily plastically deform the material to failure.

The selection of the particular range of spheroidized microstructures used in these experiments was fortuitous because it demonstrated that

microstructural variations that change ductility only have a positive effect on erosion behavior over a limited range. When that range is exceeded, the erosion behavior reverts to a basic function of strength or hardness; the stronger materials eroding less.



## CONCLUSIONS

The following conclusions can be drawn from the investigation:

1. Microstructure plays a role in the solid particle erosion of ductile alloys. In both steels tested, the erosion rate was directly related to the distribution of hard, brittle and soft, ductile phases in the alloy. Within limits, the more continuous the ductile matrix was, the lower the erosion rate was. However, when the ductile matrix becomes the predominant phase and the resulting strength of the steel is markedly reduced, strength becomes the dominant factor in erosion and not ductility. In the 1075 steel, the spheroidized structure with its brittle carbide particles concentrated into spheroids interspersed in a more continuous ductile ferrite matrix eroded less than the pearlite structure where the carbide was in platelets, finely separating the areas of ductile ferrite. In two of the three 1020 steel tests, the greater the distance between brittle carbide spheroids, the smaller the amount of erosion. However, when particle spacing got too great the steel reverted to the high erosion rate of the low strength ferrite matrix.

2. The erosion resistance of the 1075 steel and the two harder 1020 steel samples varied inversely with hardness rather than directly, as generally reported in the literature.

3. The pearlitic structure of the 1075 cracked at and near the surface, along planes of carbide while the spheroidized steel only cracked at a depth of about 20  $\mu\text{m}$  below the surface. The cracks

initiated at carbide particle-ferrite matrix interfaces and propagated through the ferrite matrix.

4. Hydrostatic compression occurs directly beneath the point of impact of a particle, as evidenced by the bending of some of the carbide plates of the pearlite without their fracturing.

5. There is a definite lower erosion rate threshold region that occurs before higher rate, steady state erosion begins.

6. Work hardening of the surface of the spheroidized 1075 steel by rolling prior to erosion testing increases the amount of erosion that occurs during the initial period of material loss.

## REFERENCES

1. I. Finnie, An Experimental Study of Erosion, Proc. Soc. Exptl. Stress Anal., 17 (2) (1960) 65.
2. I. Finnie, Erosion of Surfaces by Solid Particles, Wear, 3 (1960) 87.
3. C. Smeltzer, M. Gulden, W. Compton, Mechanisms of Metal Removal by Impacting Dust Particles, Journal of Basic Engineering, Transactions of the A.S.M.E., Sept. (1970) 639.
4. G. Grant and W. Tabakoff, Erosion Prediction in Turbomachinery Due to Environmental Solid Particles, Proceedings A.I.A.A. 12th Aerospace Science Meeting, 9, (1974).
5. A. MacNab, Erosion Problems in Coal Gasification Processes, Speech given at ASM-AIME Material Science Symposium, Cincinnati, (1975).
6. I. Finnie, Some Observations on the Erosion of Ductile Metals, Wear, 19 (1972) 81.
7. J. Bitter, A Study of Erosion Phenomena, Part One, Wear, 6 (1963) 5.
8. J. Bitter, A Study of Erosion Phenomena, Part Two, Wear, 6 (1963) 169.
9. J. Neilson, A. Gilchrist, Erosion by a Stream of Solid Particles, Wear, 11 (1968) 111.
10. J. Goodwin, W. Sage, G. Tilly, Study of Erosion by Solid Particles, Proceedings, The Institute of Mechanical Engineers, 184, Part 1.

11. G. Tilly, A Two Stage Mechanism of Ductile Erosion, *Wear*, 23 (1973) 87.
12. I. Hutchings and R. Winter, Particle Erosion of Ductile Metals: A Mechanism of Material Removal, *Wear*, 27 (1974) 121.
13. R. Winter and I. Hutchings, The Role of Adiabatic Shear in Solid Particle Erosion, *Wear*, 34 (1975) 141.
14. N. Suh, the Delamination Theory of Wear, *Wear*, 25 (1973) 111.
15. G. Sheldon and A. Kanhere, An Investigation of Impingement Erosion Using Single Particles, *Wear*, 21 (1972).
16. L. Ives and A. Ruff, Transmission and Scanning Electron Microscopy Studies of Deformation at Erosion Impact Sites, Proceedings, International Conference on Wear of Materials, April 25-28, A.S.M.E., (1977) 392.
17. D. Kleist, One Dimensional - Two Phase Particulate Flow, Master's Thesis, Department of Mechanical Engineering, University of California, Berkeley (1977).
18. A. Ruff, L. Ives, Measurement of Solid Particle Velocity in Erosive Wear, *Wear*, 35 (1975) 195.
19. P. Hurricks, Some Metallurgical Factors Controlling the Adhesive and Abrasive Wear Resistance of Steels. A Review, *Wear*, 26 (1973) 285.

## FIGURE CAPTIONS

- Figure 1. Plots of erosion rate (grams removed/grams of impacting particles) versus angle of impingement, (degrees) of a) a typical ductile alloy, and b) typical brittle material.
- Figure 2. Scanning electron micrographs of 1075 steel in the coarse pearlite, fine pearlite, and spheroidized microstructures.
- Figure 3. Photograph of room temperature erosion tester.
- Figure 4. Schematic diagram of room temperature erosion tester.
- Figure 5. A. Schematic diagram of erosion tester with rotary particle velocity testing device attached.  
B. Description of variables for particle velocity measurements.
- Figure 6. Plot of engineering stress versus engineering strain for 1075 steel – coarse pearlite and spheroidized.
- Figure 7. Plot of erosion rate (mg/g) versus amount of impacting particles (gm) for 1075 steel – coarse pearlite, fine pearlite, and spheroidized – using 240  $\mu\text{m}$  diameter SiC.  
 $V_p = 30.5 \text{ mps (100 fps)}$ ,  $\alpha = 30^\circ$ .
- Figure 8. Plot of erosion rate (mg/g) versus amount of impacting particles (gm) for 1075 steel – coarse pearlite, fine pearlite, and spheroidized – using 240  $\mu\text{m}$  SiC.  
 $V_p = 61 \text{ mps (200 fps)}$ ,  $\alpha = 30^\circ$ .

- Figure 9. Plot of erosion rate (mg/g) versus angle of impingement (degrees) for 1075 steel in the coarse pearlite, fine pearlite, and spheroidized microstructures using 240  $\mu\text{m}$  SiC.  $V_p = 30.5$  mps (100 fps).
- Figure 10. Plot of erosion rate (mg/g) versus angle of impingement (degrees) for 1075 steel in the coarse pearlite, fine pearlite, and spheroidized microstructures using 240  $\mu\text{m}$  SiC.
- Figure 11. Photomicrograph of single particle impact crater on 1075 steel (coarse pearlite) using 240  $\mu\text{m}$  SiC.  $V_p = 61$  mps (200 fps),  $\alpha = 15^\circ$ . Stereo pair can be viewed with stereo viewer found in back cover of ASM Handbook, Vol. 9.
- Figure 12. Photomicrograph of a single particle impact crater on 1075 steel (coarse pearlite) using 240  $\mu\text{m}$  SiC.  $V_p = 107$  mps (350 fps),  $\alpha = 15^\circ$ .
- Figure 13. Photomicrograph of a single particle impact crater on 1075 steel (spheroidized) using 240  $\mu\text{m}$  SiC (stereo pair included):  $V_p = 61$  mps (200 fps),  $\alpha = 15^\circ$ .
- Figure 14. a) and b) Photomicrographs of cross sections of single particle impact craters formed in 1075 steel (coarse pearlite) using 1200  $\mu\text{m}$  diameter SiC.  $V_p = 30.5$  mps (100 fps),  $\alpha = 90^\circ$ .
- Figure 15. a) Scanning electron micrograph of 1075 steel (coarse pearlite) after multiple erosion with 240  $\mu\text{m}$  SiC.  $V_p = 61$  mps (200 fps),  $\alpha = 30^\circ$ .

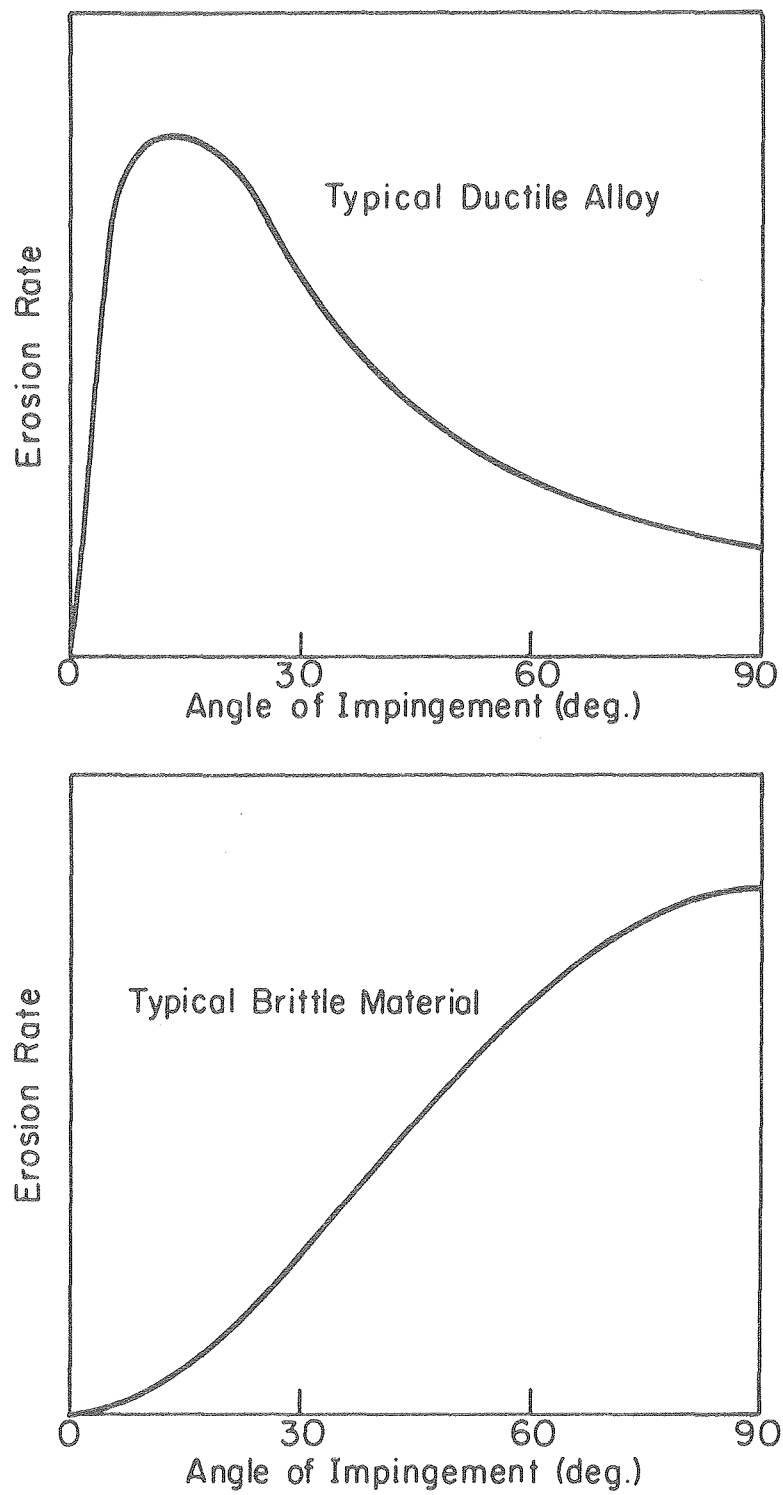
Figure 16. Scanning electron micrograph of cross section of 1075 steel (spheroidized) after multiple particle erosion with  $240\text{ }\mu\text{m SiC}$ .  $V_p = 61\text{ mps (200 fps)}$ ,  $\alpha = 30^\circ$ .

Figure 17. a) and b) Scanning electron micrographd of cross sectiond of 1075 steel (coarse pearlite) sample after multiple erosion with  $240\text{ }\mu\text{m SiC}$   $V_p = 61\text{ mps (200 fps)}$ ,  $\alpha = 30^\circ$ .

Figure 18. Spheroidized 1020 steel with smallest carbide particle size, smallest particle spacing and largest number of particles.

Figure 19. Spheroidized 1020 steel with intermediate carbide particle size, greater particle spacing and fewer particles.

Figure 20. Spheroidized 1020 steel with very large sized particles, great particle spacing and relatively few particles.

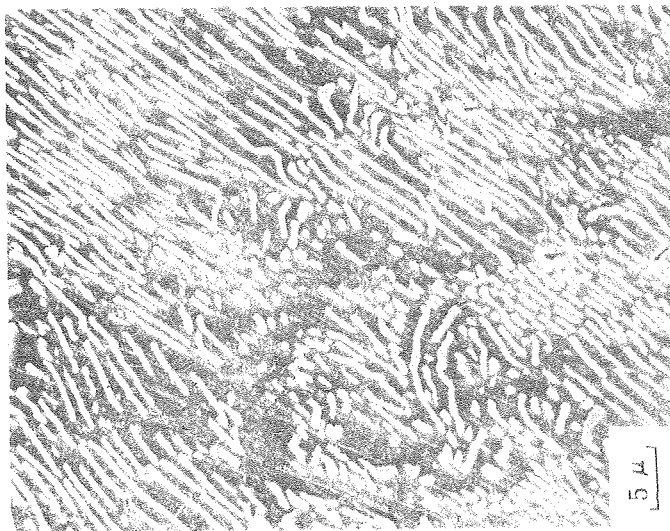


XBL 775-5511

Figure 1

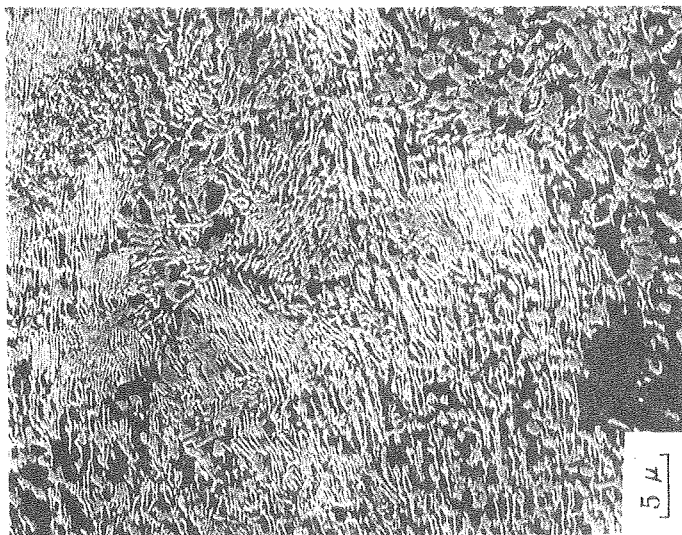


# EROSION OF 1075 STEEL



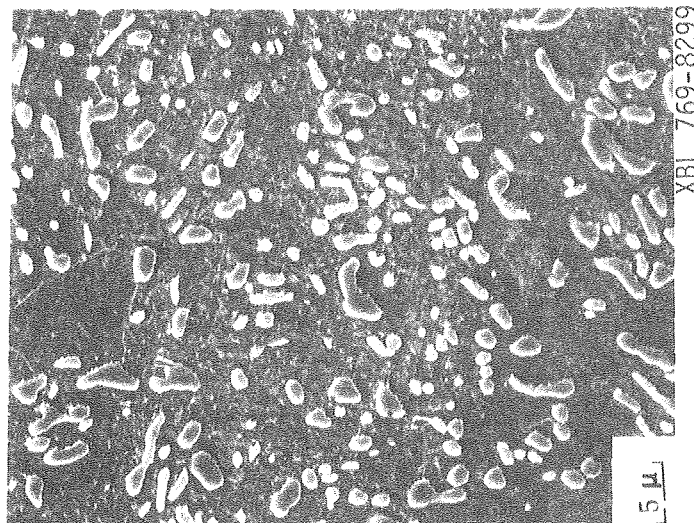
COARSE PEARLITE

Hardness -  $R_B$  90  
Lamellar Spacing  $\sim 1 \mu m$



FINE PEARLITE

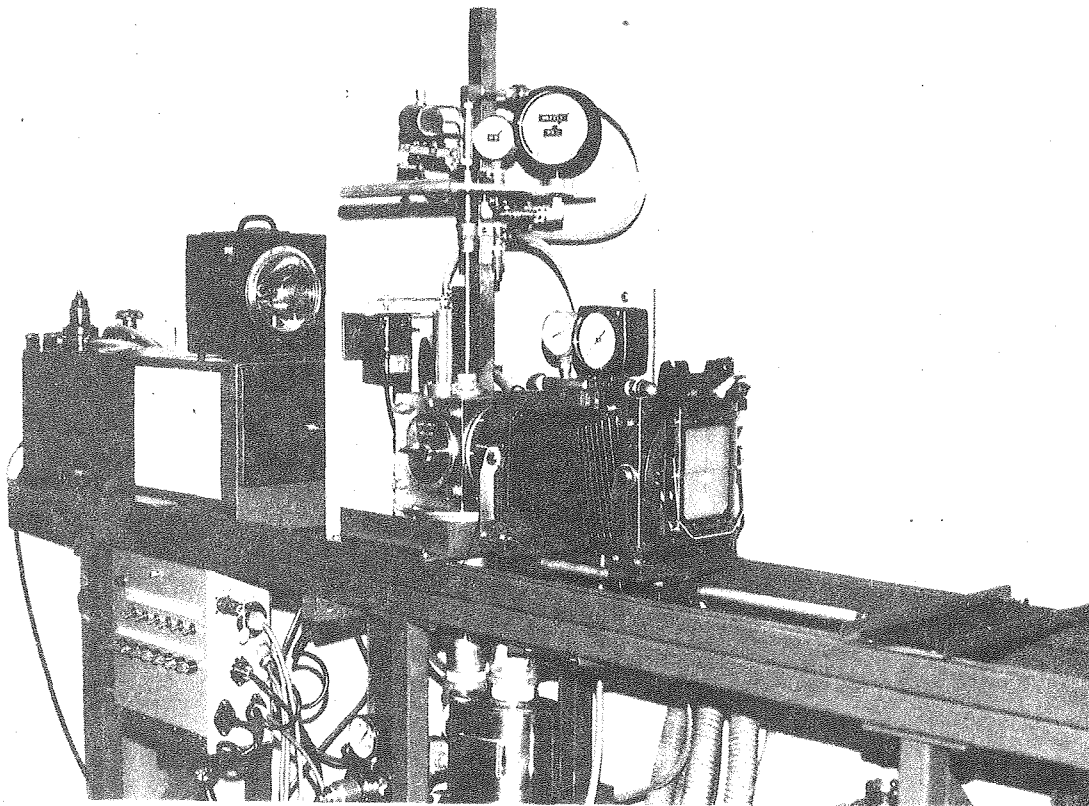
Hardness -  $R_B$  99 ( $R_C$  20)  
Lamellar Spacing  $\sim 0.25 \mu m$



SPHEROIDIZED

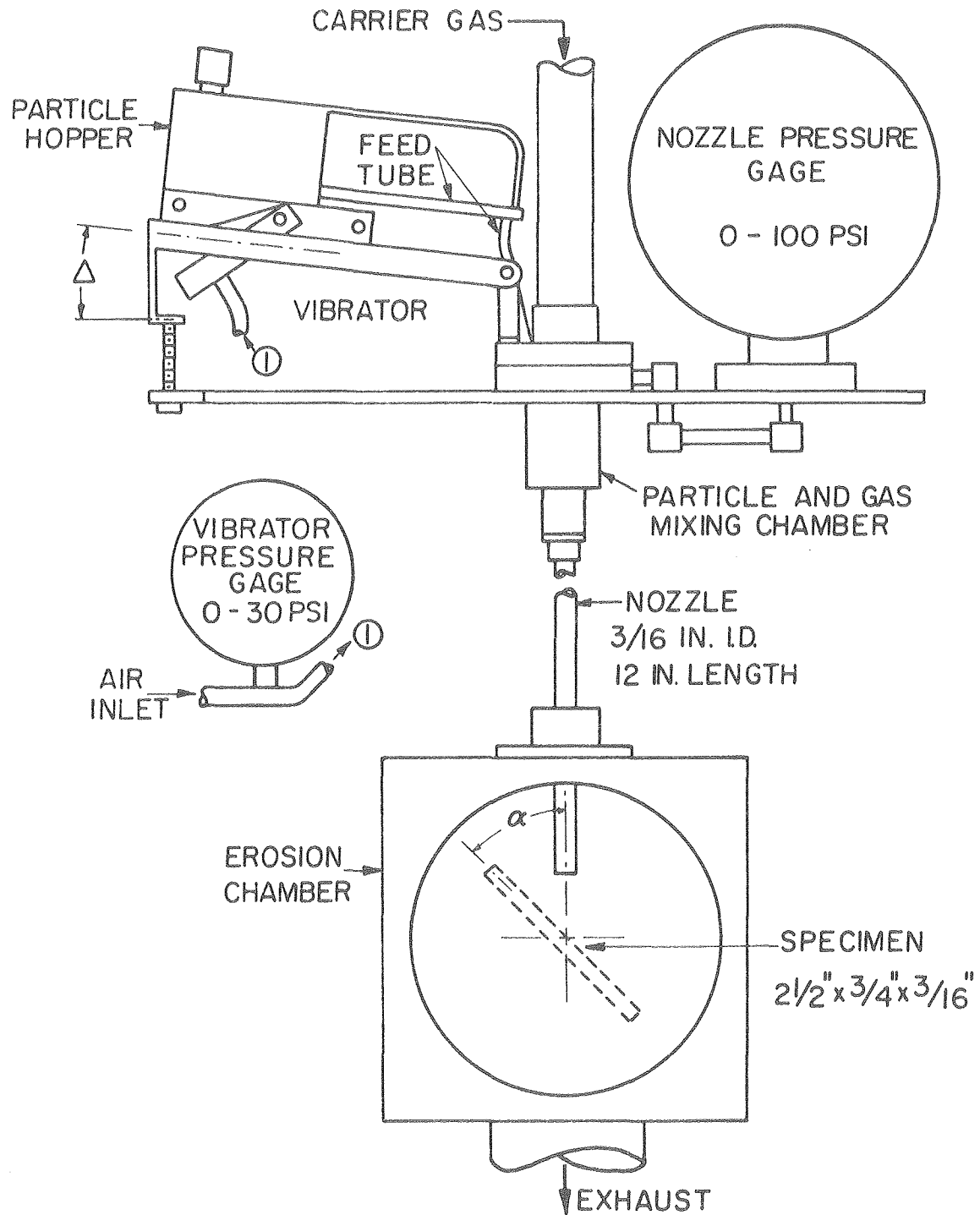
Hardness -  $R_B$  79  
Sphere Diameter  $\sim 1.25 \mu m$

Figure 2



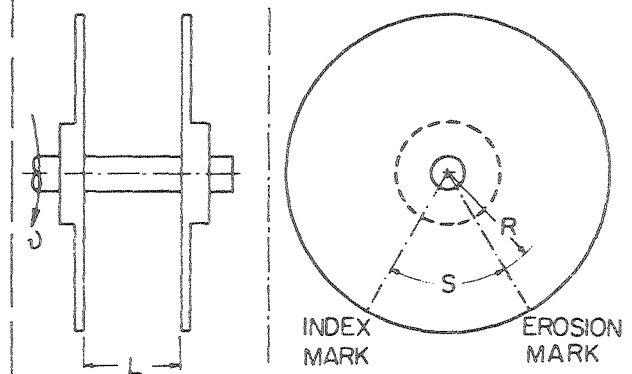
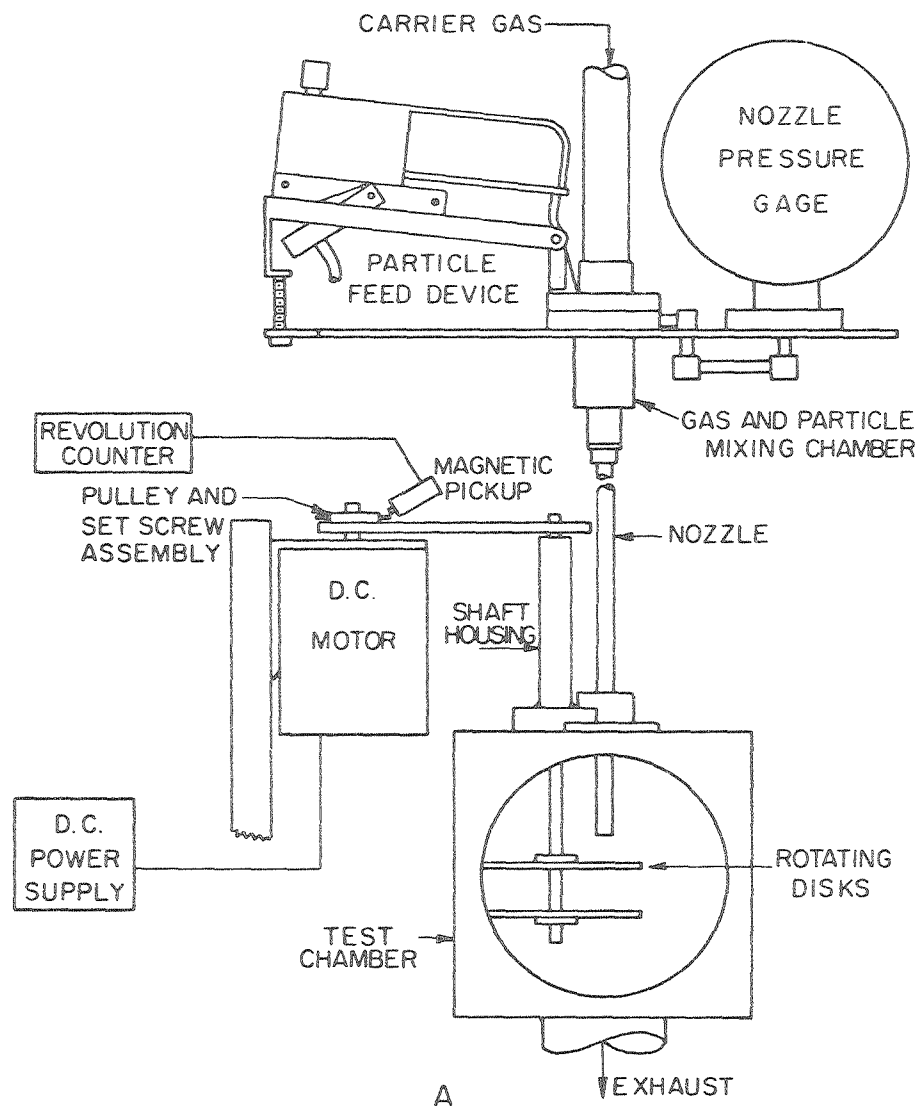
CBB 763-2073

Figure 3



XBL775-5525

Figure 4



$L$  = DISK SEPARATION  
 $S$  = ARC LENGTH BETWEEN EROSION MARKS  
 $R$  = RADIUS TO ARC LENGTH  
 $\omega$  = ANGULAR VELOCITY - REV/SEC  
 $V_p$  = PARTICLE VELOCITY  
 $= 2\pi R\omega L/S$

XBL 775-5524

Figure 5

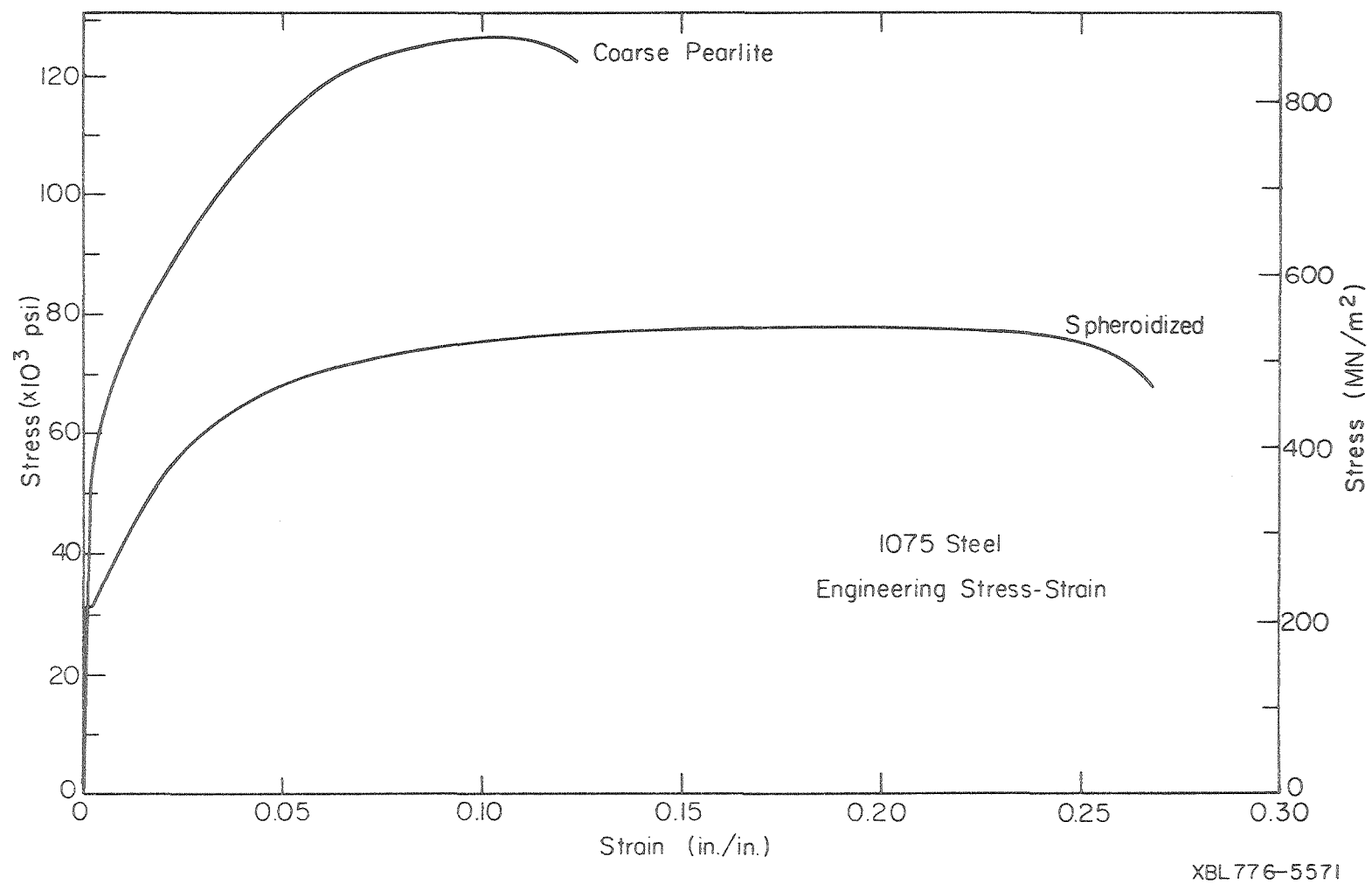
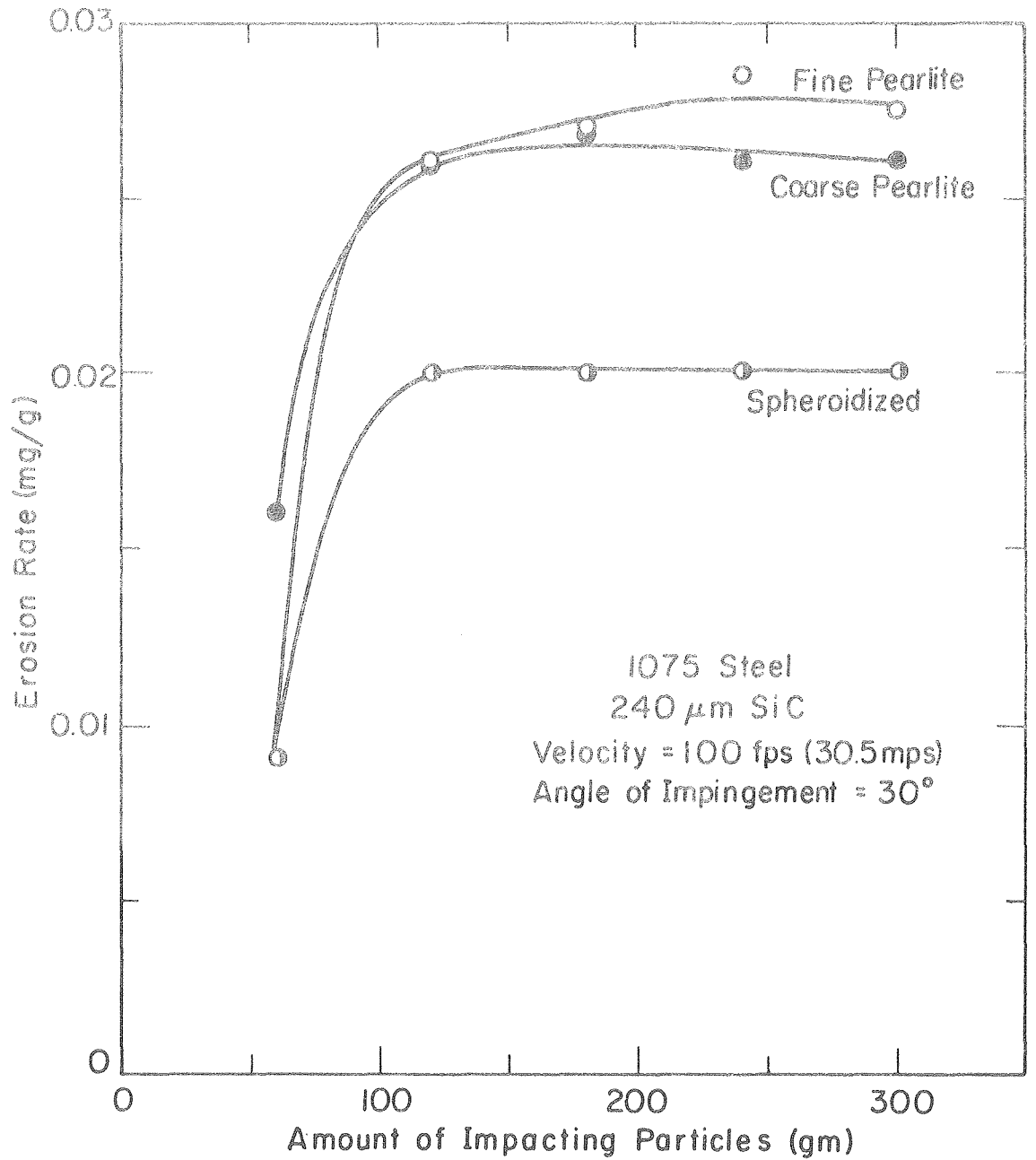
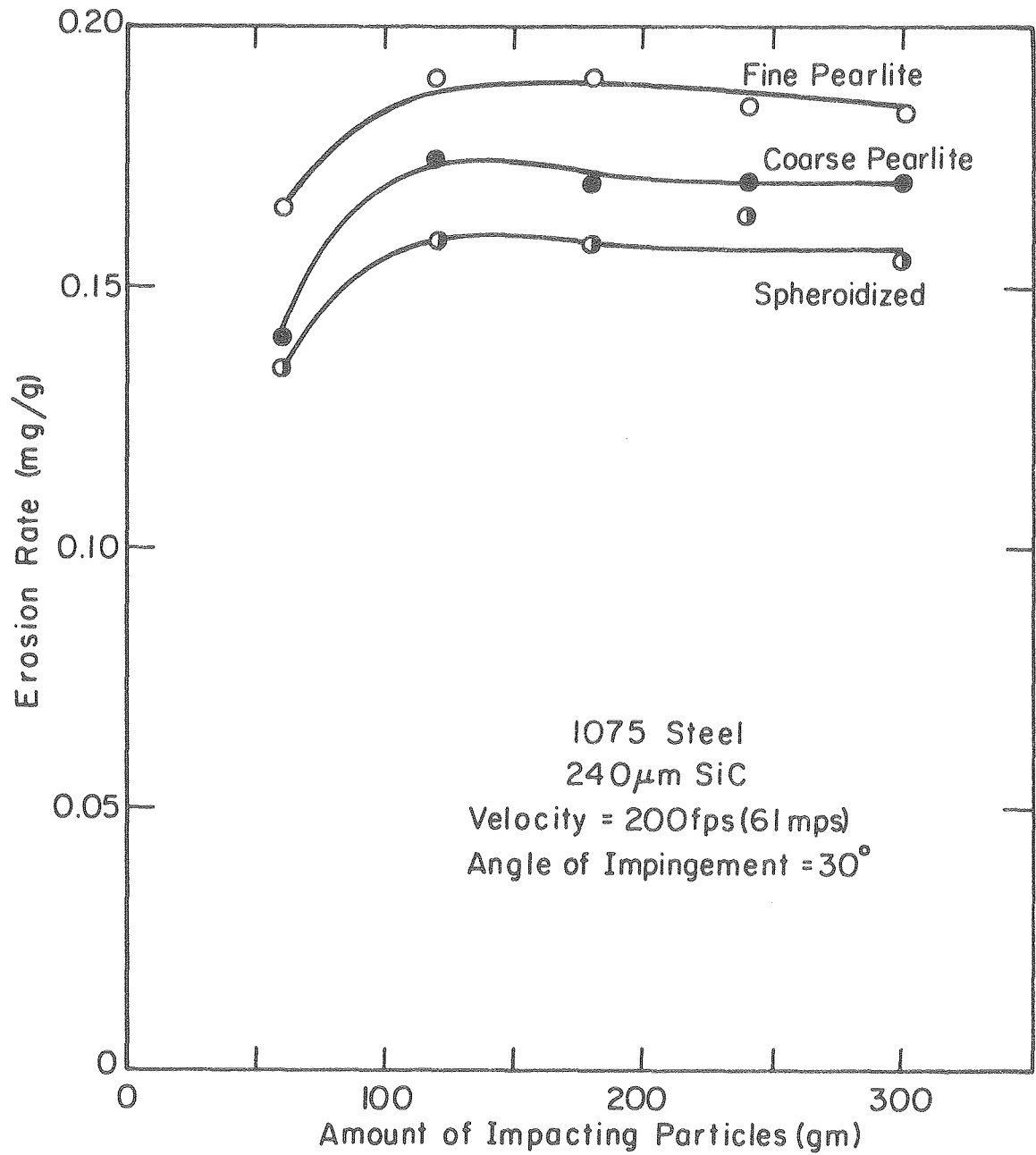


Figure 6



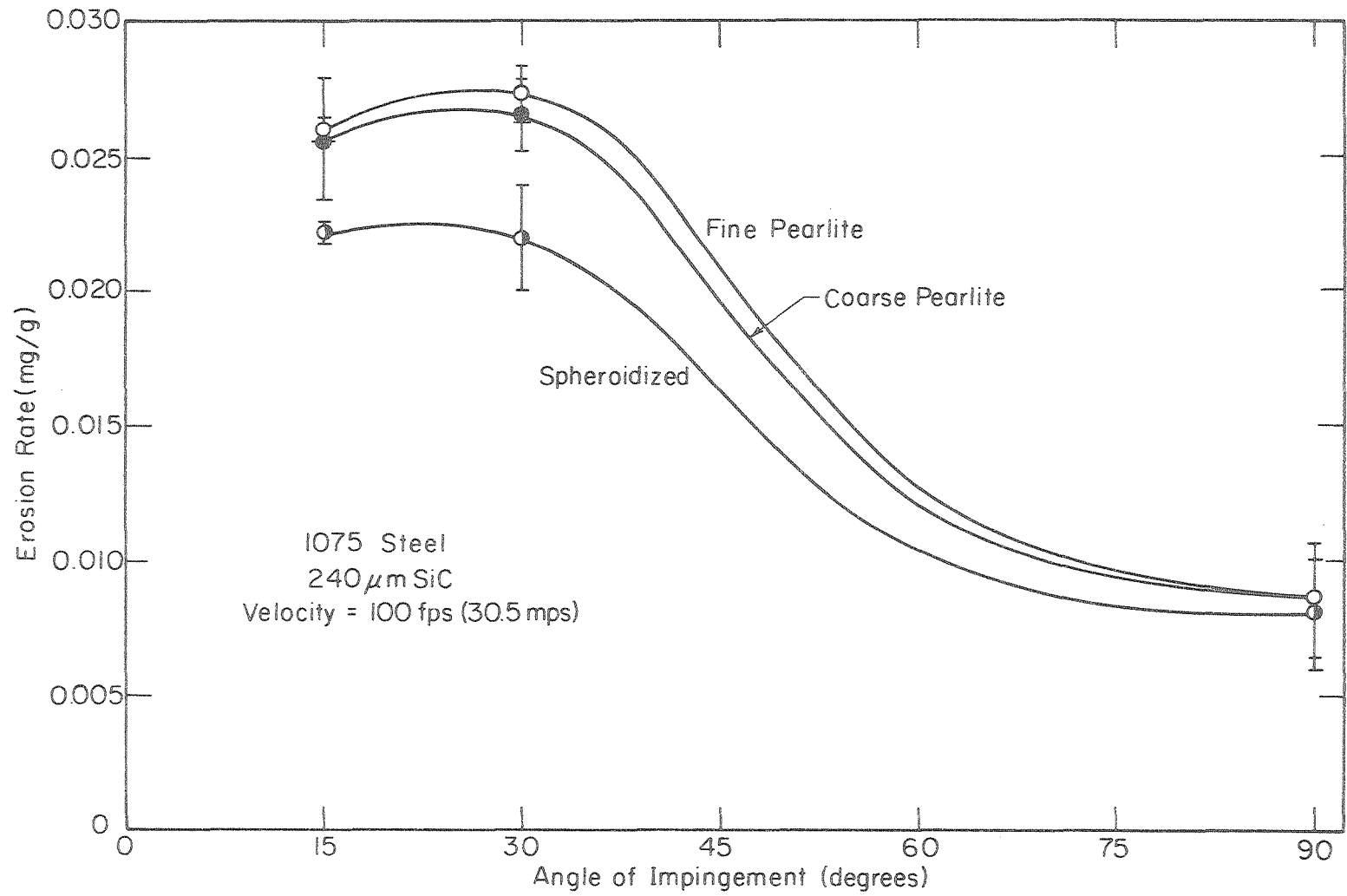
XBL775-5486

Figure 7



XBL 7 75-5493

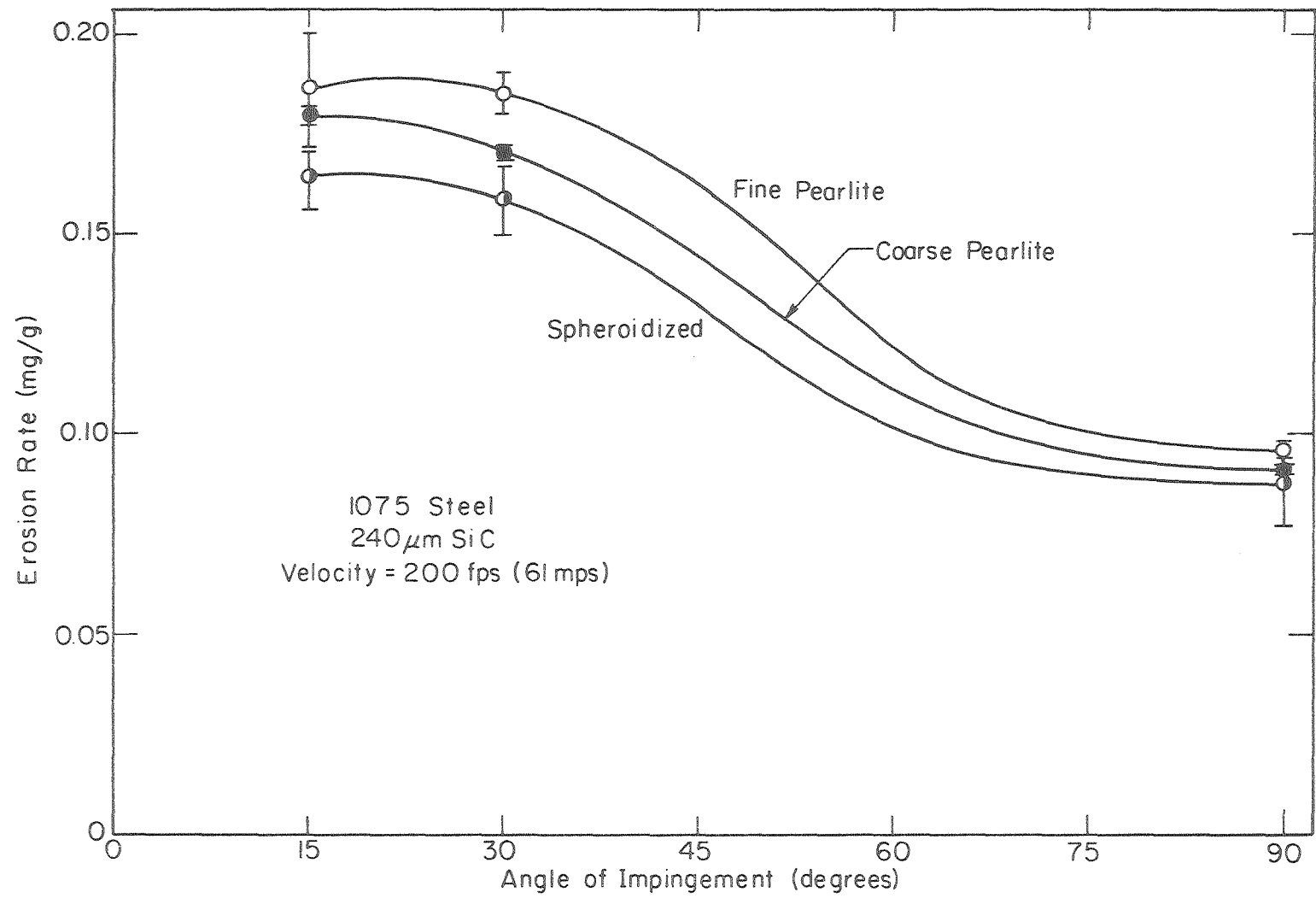
Figure 8



XBL776-5569

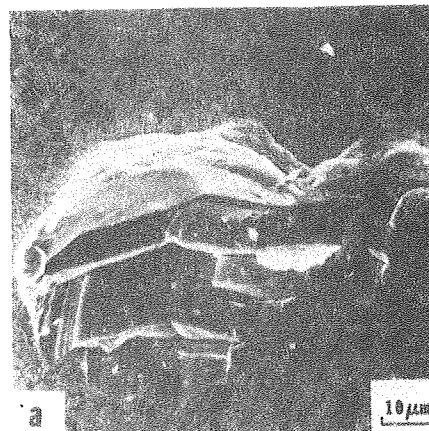
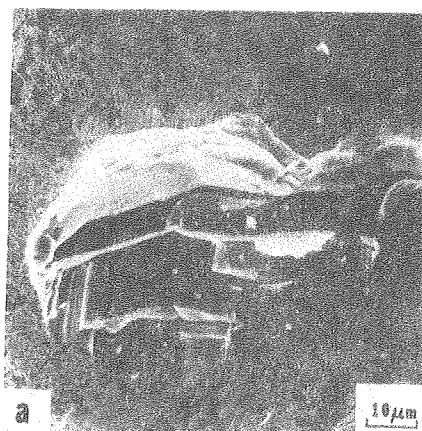
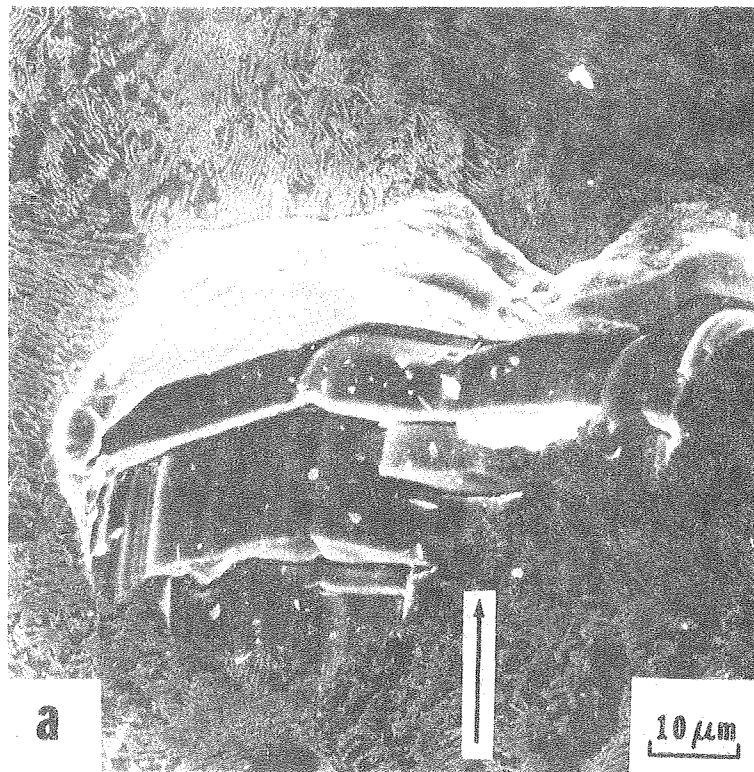
Figure 9





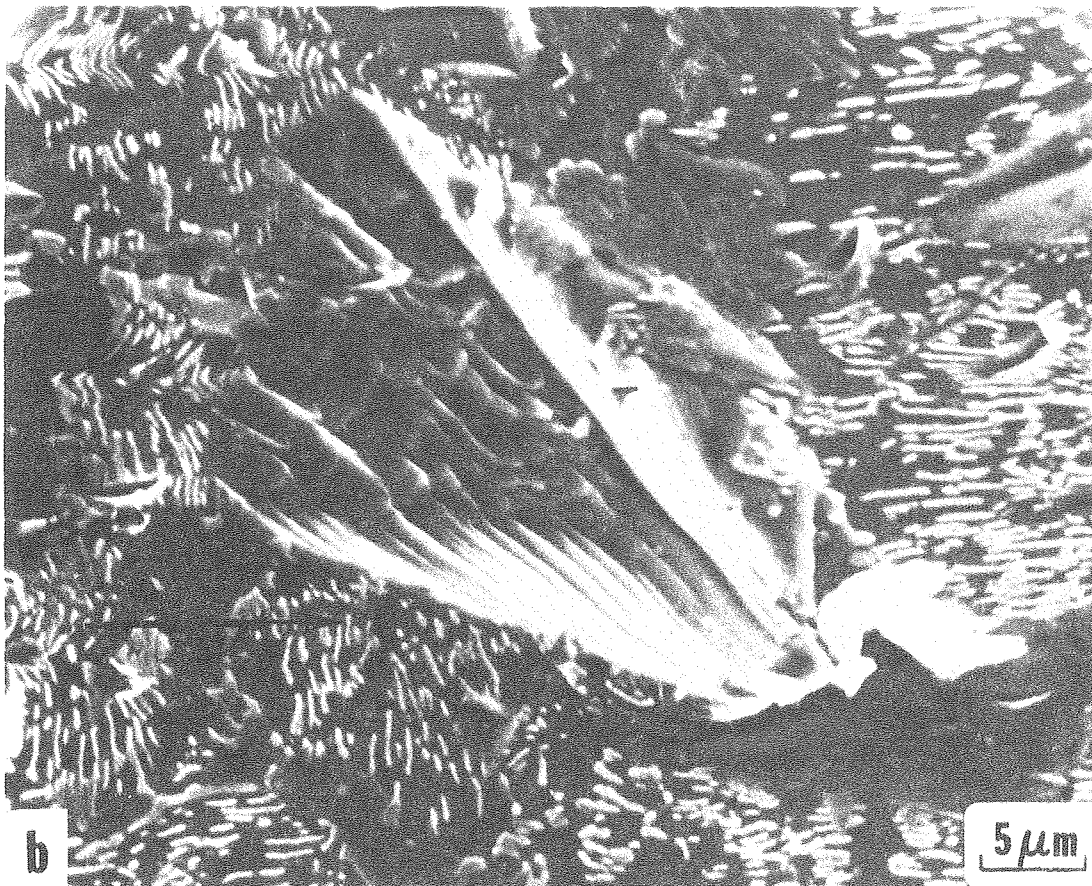
XBL776-5568

Figure 10



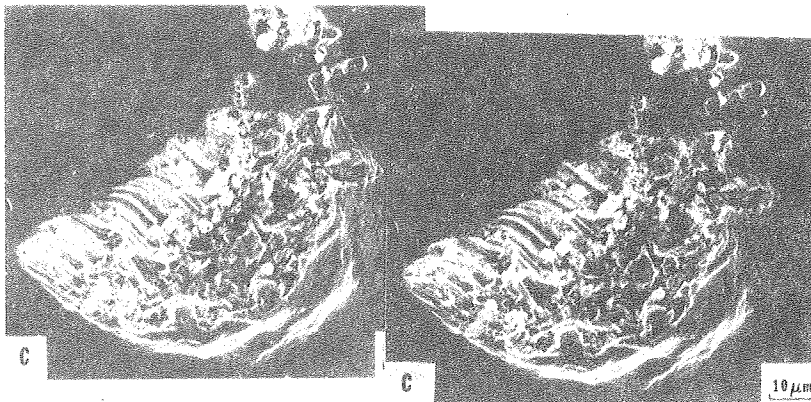
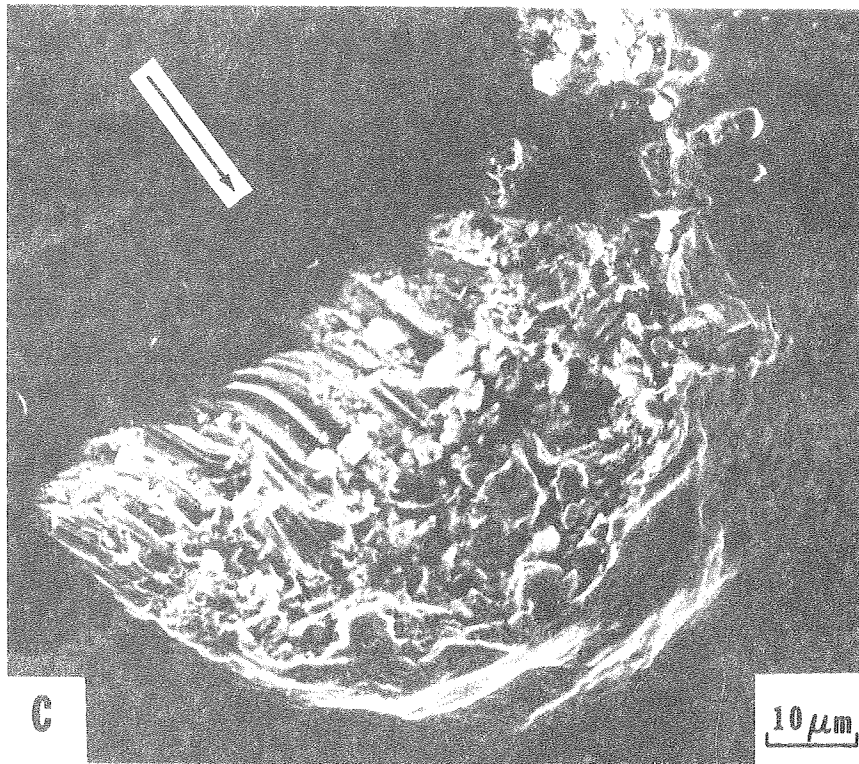
XBB 776-5505

Figure 11



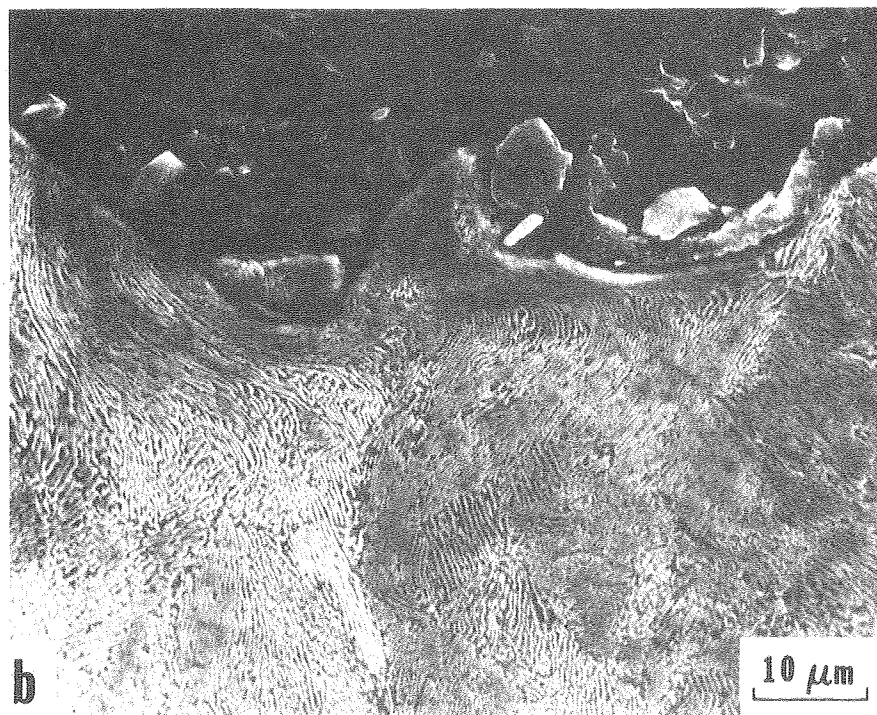
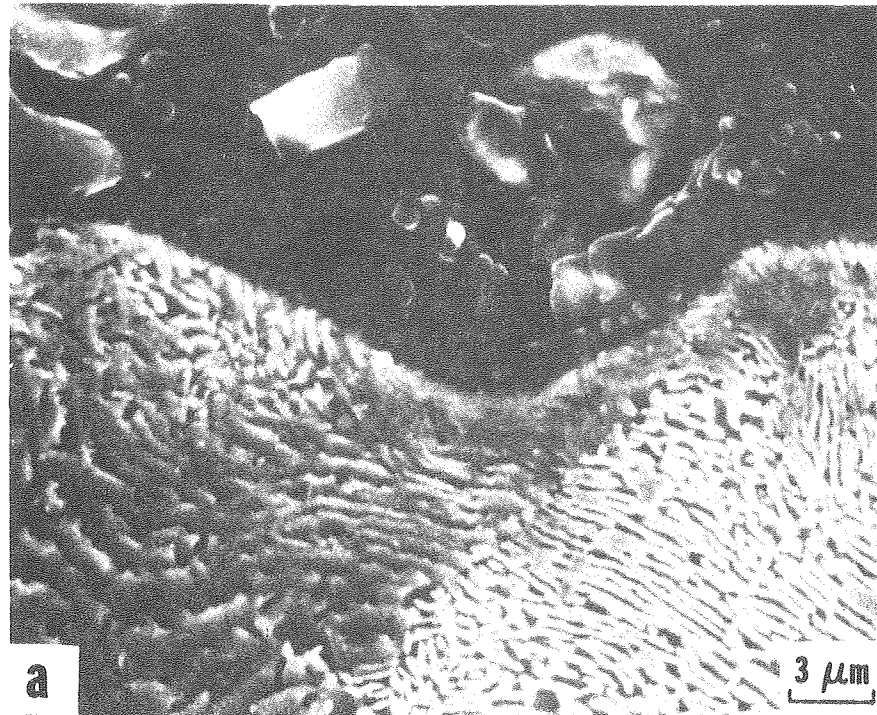
XBB 776-5635

Figure 12



XBB 776-5506

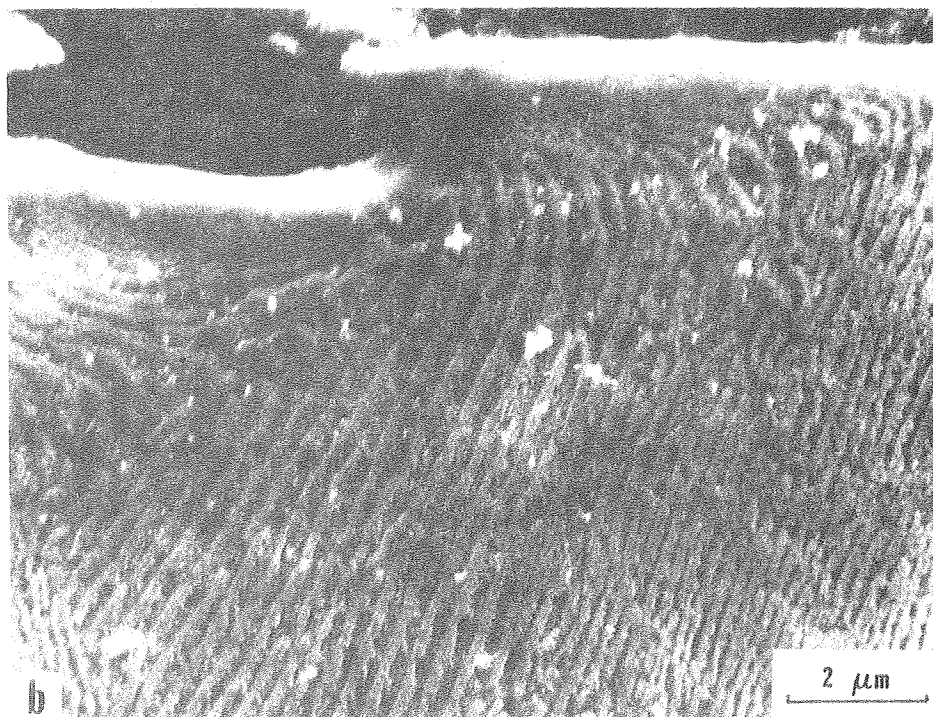
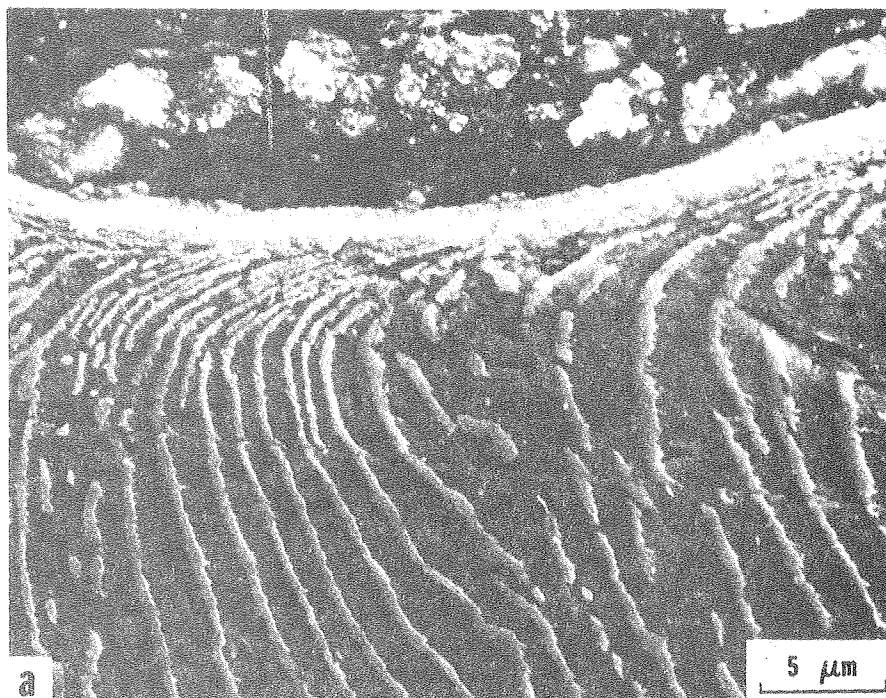
Figure 13



XBB 775-5272

Figure 14





XBB 775-5258

Figure 15

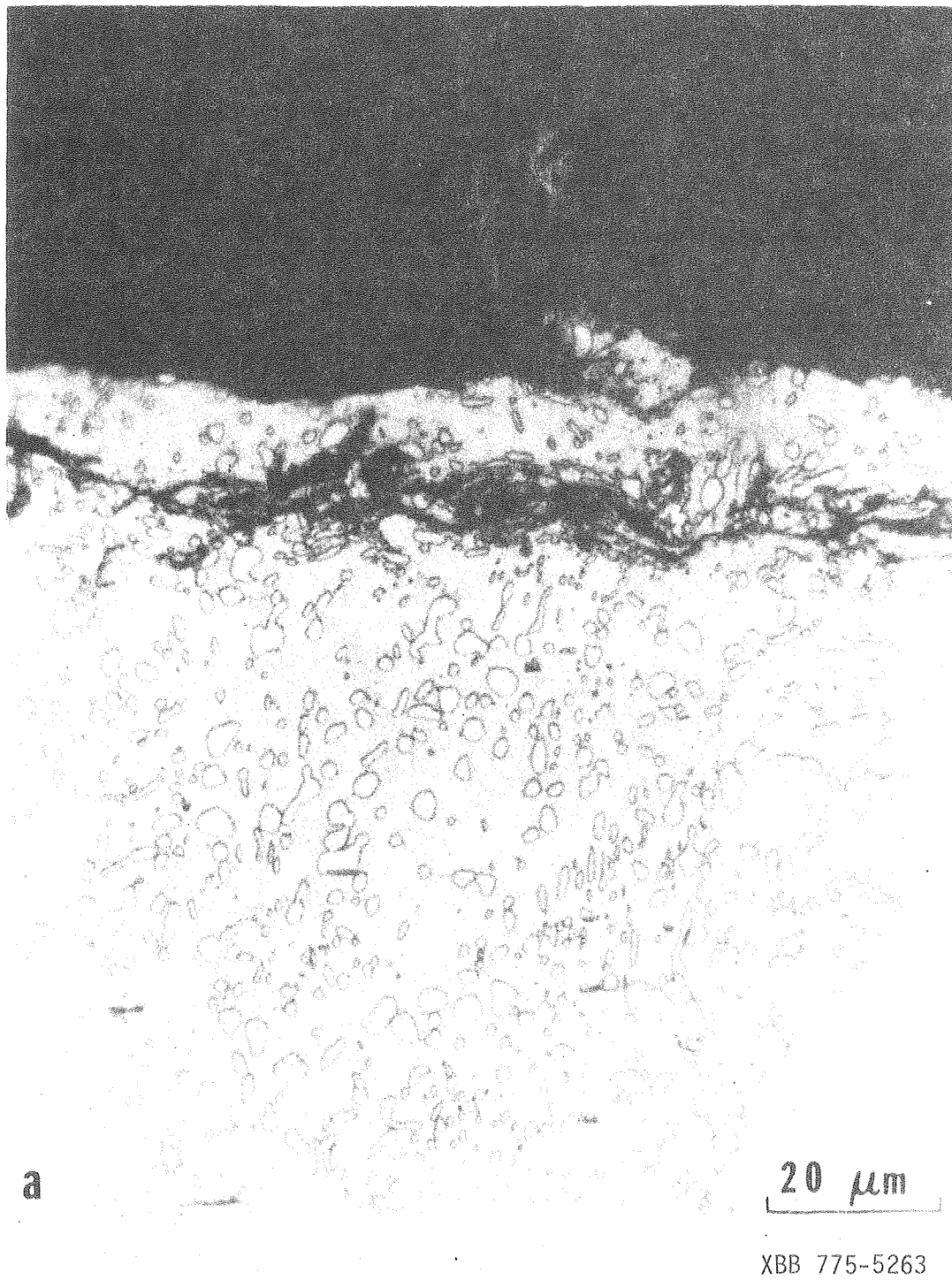
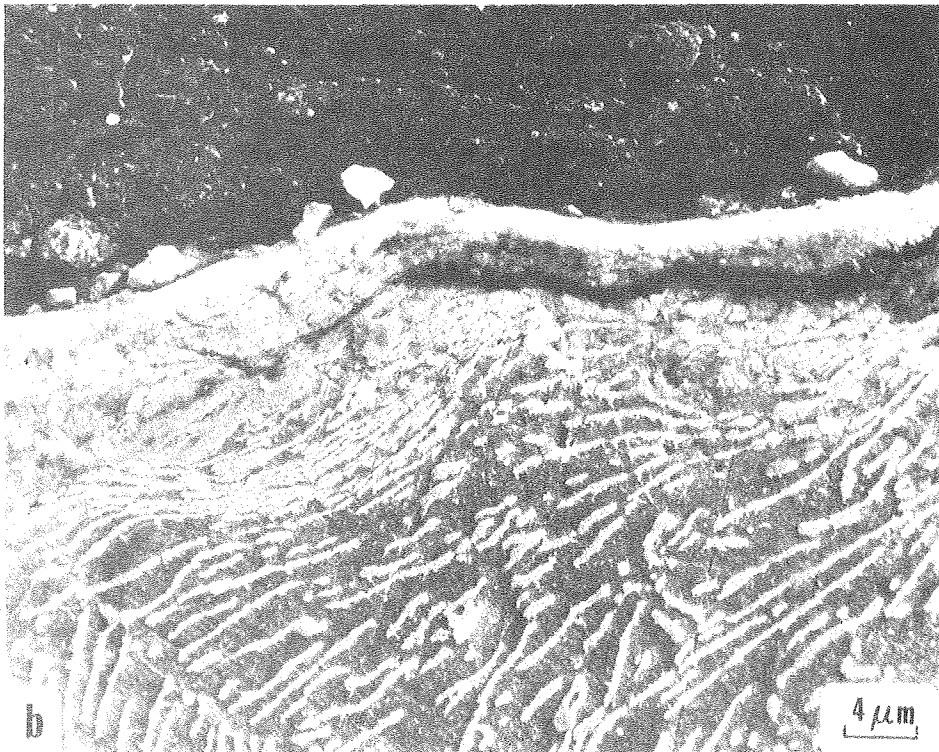
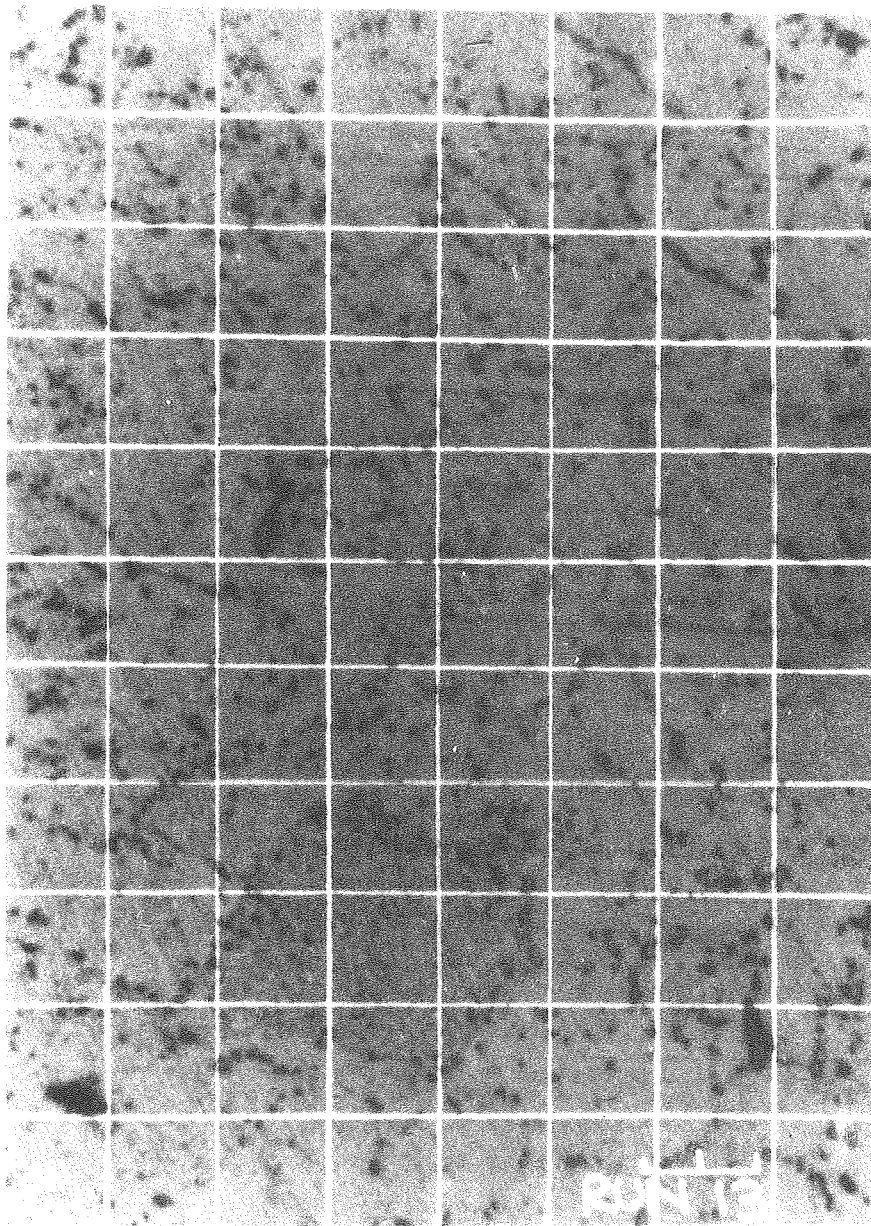


Figure 16



XBB 775-5270

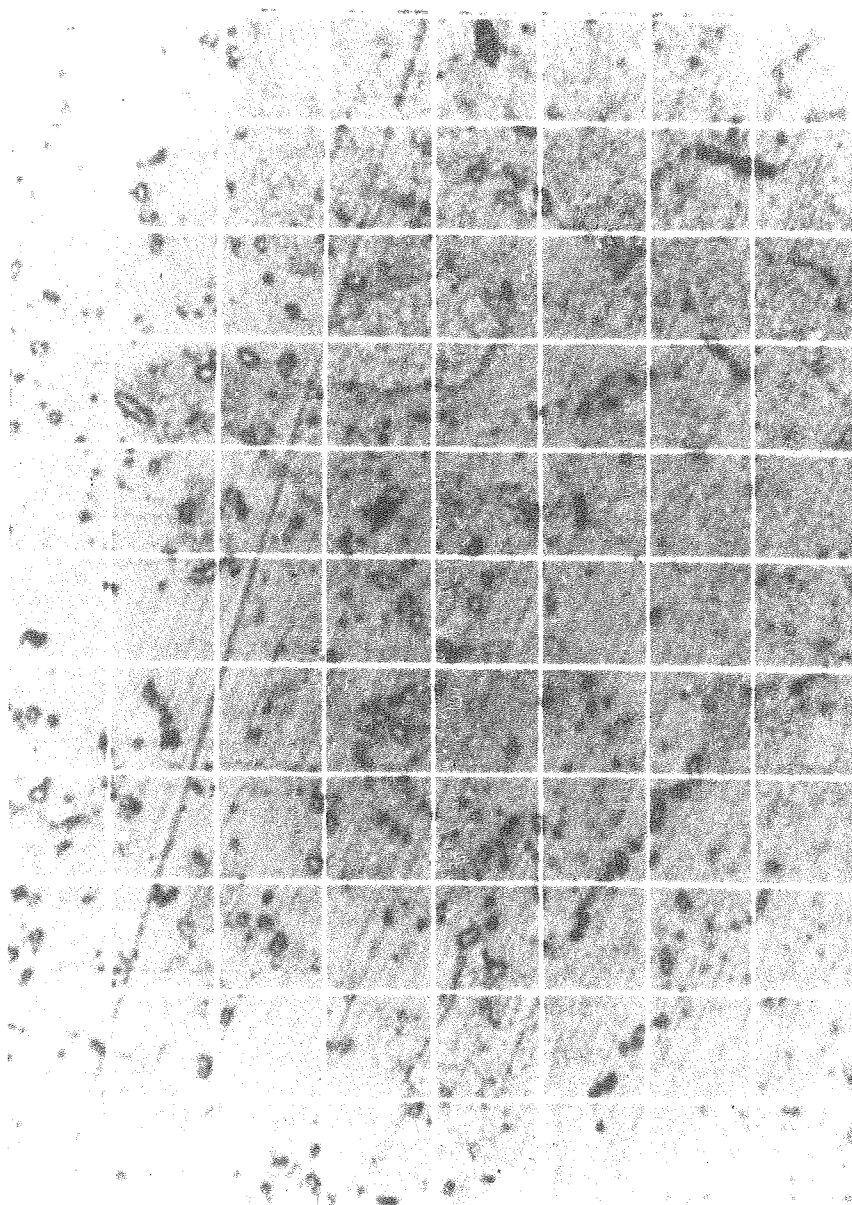




XBB 799-12730

AVERAGE PARTICLE SPACING	3.40 MICRONS
AVERAGE PARTICLE SIZE	.5 MICRONS
MINIMUM PARTICLE SIZE	.1 MICRON
MAXIMUM PARTICLE SIZE	2 MICRONS

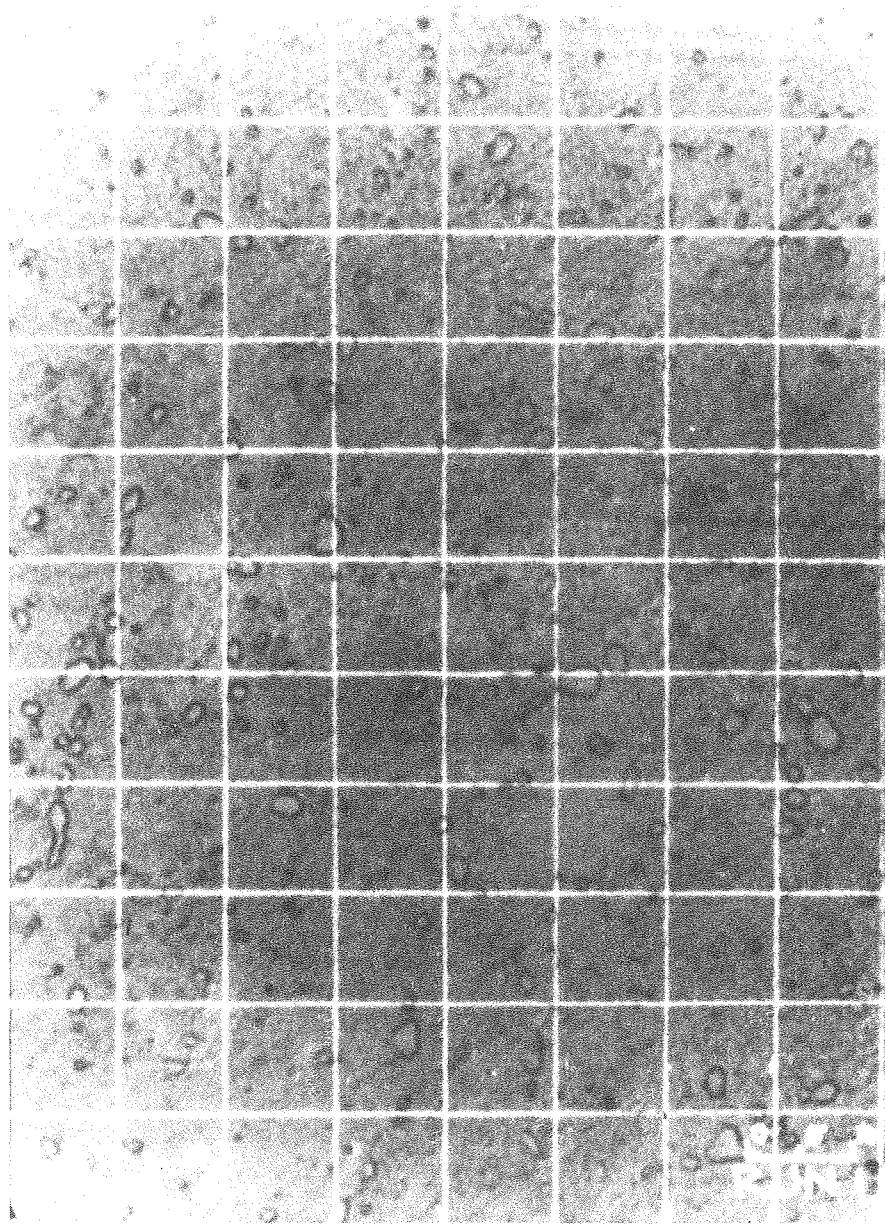
Figure 18



XBB 799-12729

AVERAGE PARTICLE SPACING	5.67	MICRONS
AVERAGE PARTICLE SIZE	1	MICRON
MINIMUM PARTICLE SIZE	.5	MICRONS
MAXIMUM PARTICLE SIZE	4	MICRONS

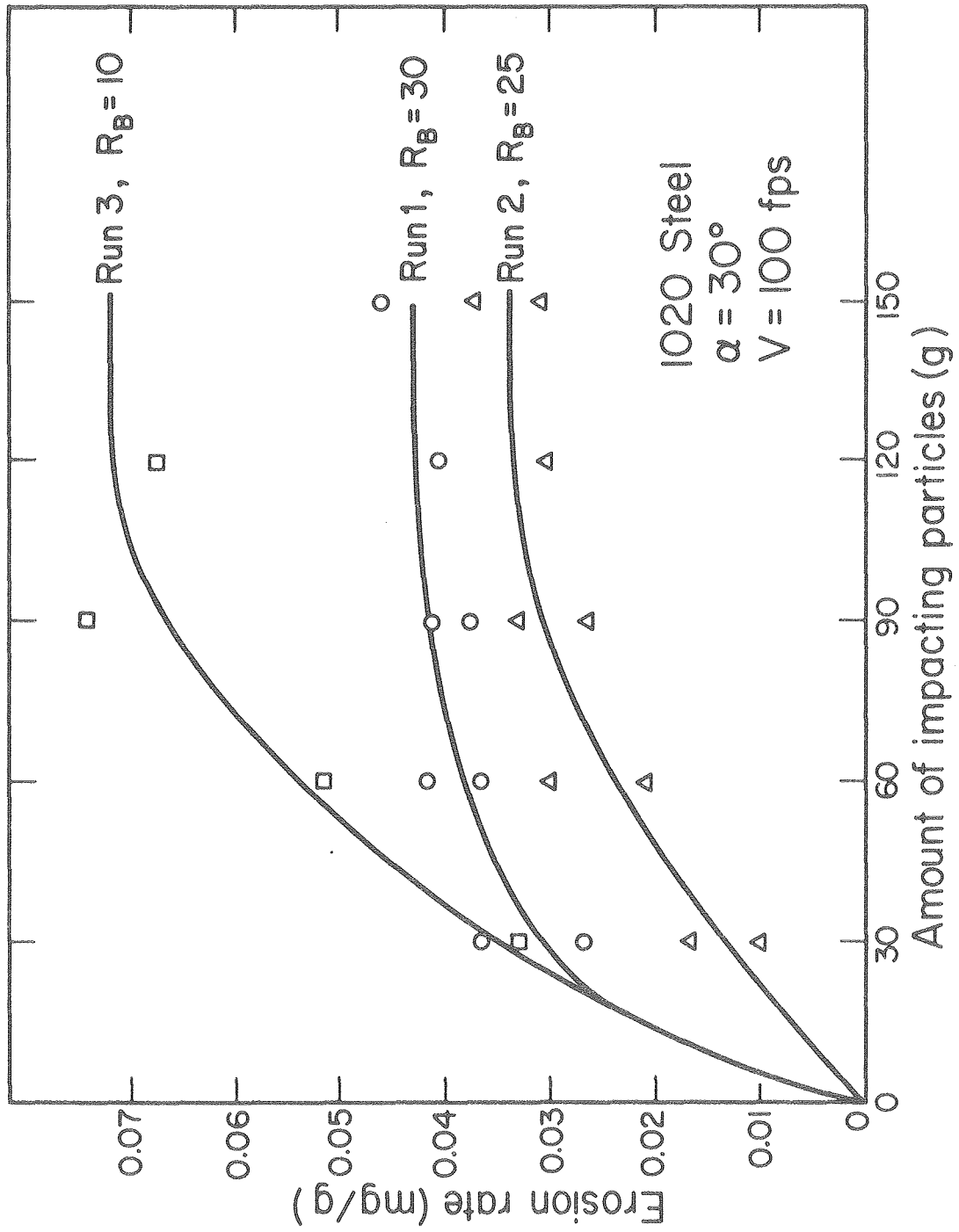
Figure 19



XBB 799-12728

AVERAGE PARTICLE SPACING	10 MICRONS
AVERAGE PARTICLE SIZE	3 MICRONS
MINIMUM PARTICLE SIZE	1 MICRON
MAXIMUM PARTICLE SIZE	5 MICRONS

Figure 20



XBL 804-700

Figure 21